Available online at www.sciencedirect.com
SCIENCE DIRECT®
Journal of Computational Physics 197 (2004) 299–340
JOURNAL OF COMPUTATIONAL PHYSICS
www.elsevier.com/locate/jcp

Finite-volume compact schemes on staggered grids

M. Piller *, E. Stalio

Dipartimento di Ingegneria Navale, del Mare e per l'Ambiente - Sezione di Fisica Tecnica, Università degli Studi di Trieste, via A. Valerio, 10, 34127 Trieste, Italy

Received 1 November 2002; received in revised form 23 October 2003; accepted 24 October 2003
Available online 22 January 2004

Abstract

Compact finite-difference schemes have been recently used in several Direct Numerical Simulations of turbulent flows, since they can achieve high-order accuracy and high resolution without exceedingly increasing the size of the computational stencil. The development of compact finite-volume schemes is more involved, due to the appearance of surface and volume integrals. While Pereira et al. [J. Comput. Phys. 167 (2001)] and Smirnov et al. [AIAA Paper, 2546, 2001] focused on collocated grids, in this paper we use the staggered grid arrangement. Compact schemes can be *tuned* to achieve very high resolution for a given formal order of accuracy. We develop and test high-resolution schemes by following a procedure proposed by Lele [J. Comput. Phys. 103 (1992)] which, to the best of our knowledge, has not yet been applied to compact finite-volume methods on staggered grids. Results from several one- and two-dimensional simulations for the scalar transport and Navier–Stokes equations are presented, showing that the proposed method is capable to accurately reproduce complex steady and unsteady flows.

Keywords: Compact schemes; Finite-volume; Staggered grid

1. Introduction

Turbulent flows are characterized by a wide range of time and length scales [1], which can be numerically resolved by using small grid spacings and time steps. Resolution can also be improved by using highly accurate schemes, either in space or in time. This work focuses on the application of compact finite-volume schemes (CFV schemes hereafter) to the numerical simulation of thermo-fluid dynamics problems.

Several authors [2–7] have contributed to the development of compact finite-difference schemes; they can achieve high-order accuracy and high resolution without exceedingly increasing the size of the computational stencil, and are more flexible in terms of geometry and boundary conditions than spectral methods. The computational efficiency of compact schemes is highly dependent on the specific implementation. For example, Meinke et al. [8] report that the computational cost of solving the

* Corresponding author. Tel.: +39-040-558-3502; fax: +39-040-572033.
E-mail addresses: piller@univ.trieste.it (M. Piller), stalio@univ.trieste.it (E. Stalio).

0021-9991/$ - see front matter
doi:10.1016/j.jcp.2003.10.037

three-dimensional compressible Navier–Stokes equations, by a sixth-order compact finite-difference scheme, is about 1.5 times higher than using a combination of a second-order scheme for the viscous term and the AUSM upwind scheme [9] for the advective term. Meinke et al. [8] use a five-step explicit Runge–Kutta time-stepping scheme. Compact finite-difference schemes have been recently used in several DNS of turbulent flows. Few selected examples include the DNS of a compressible, subsonic boundary layer around an airfoil [10], applications concerning unsteady flows in complex geometries [11] and a DNS of jet noise [12].

As remarked by Morinishi et al. [13], experience has shown that the convective terms must conserve kinetic-energy if an incompressible, unsteady flow simulation is to be both stable and free of numerical dissipation. Lele [7] derived conservative compact finite-difference schemes on uniform grids. Second-order finite-difference and finite-volume schemes on staggered grids are known to intrinsically conserve kinetic energy, on uniform Cartesian grids [14,15]. High-order, kinetic energy conserving, finite-difference schemes on uniform staggered grids were developed by Morinishi et al. [13], and extended to non-uniform Cartesian grids by Vasilyev [15]. Nagarajan et al. [16] compared collocated and staggered compact finite-difference algorithms for the simulation of compressible flows, and showed that the staggered approach is definitely more robust, due to its better conservation properties. No investigation of the conservation properties of collocated compact finite-volume schemes has been attempted up to date, to the best of our knowledge. Another favorable property of staggered grids is that the pressure–velocity coupling is inherently enforced [17]. Pereira et al. [18] and Smirnov et al. [19] used a collocated grid arrangement; the pressure–velocity coupling was enforced by allowing for odd number of control volumes along each coordinate direction. Even though the effectiveness of this method of avoiding pressure–velocity decoupling can be analytically proved only for uniform grids and periodic or Dirichlet boundary conditions [18], the results of several simulations performed by Pereira et al. [18] and Smirnov et al. [19] do not show any unphysical oscillation, which could be attributed to pressure–velocity decoupling. A further attractive property of finite-volume and finite-difference schemes on staggered grids is that no extrapolation is needed, near boundaries where the velocity field is imposed, in order to represent the pressure gradient term in the momentum equations [17].

Although collocated grids present several advantages (lower memory requirements, easier book-keeping), in view of the above discussion we believe that the development of compact finite-volume schemes on staggered grids should deserve some attention, since they are good candidates for what concernes conservation of kinetic-energy. We use the staggered variable arrangement introduced by Harlow and Welch [14], which locate scalar variables, like pressure and temperature, at the centroid of each control volume, while the normal velocity components are assigned to the centroids of the cell faces. In addition, we devise an efficient approach for the solution of the unsteady Navier–Stokes equations. Semi-implicit time-stepping schemes, like the low storage Runge–Kutta by Le and Moin [20] and the Crank–Nicolson/Adams–Bashforth, are used in conjunction with the Alternate Direction Implicit (ADI) method [17]. The discrete conservation equations and the compact difference equations, required for the approximation of the diffusive fluxes, are solved simultaneously by using a direct method for *almost* banded coefficient matrices, developed following and extending ideas first proposed by Temperton [21].

Cell-averaged values and fluxes are assumed as main unknowns, an approach already adopted by Pereira et al. [18] and by Smirnov et al. [19]. This practice is very natural in finite-volume applications, since it avoids introducing complicate compact-quadrature formulas, which would enlarge the computational molecule and, in multi-dimensional applications, would strengthen the coupling between different coordinate directions. Point values of each quantity can be recovered from cell-averaged values once and for all at the end of a simulation, by a deconvolution process [18].

Symmetric spatial-discretization schemes are used in the interior of the computational domain, while asymmetric schemes are applied only for the discretization of Dirichlet or Neumann boundary condi-

tions. Symmetric compact schemes do not introduce numerical diffusivity, but are affected by spurious oscillations on coarse grids [7]. This characteristic of compact schemes is due to the sensitivity to aliasing errors, which affects high-resolution symmetric schemes [16]. In DNS applications, accuracy and resolution requirements limit the maximum value of the cell Péclet number, so that the appearance of wiggles is, or at least should be, a quite rare circumstance. In addition, as pointed out by Lilek and Perić [22], in common practice wiggles usually arise for values of the cell Péclet number which are higher than those expected from theory. In *critical* applications, the onset of wiggles can be kept under control by several techniques. Compact low-pass filters were first applied by Lele [7], while Jiang et al. [23] developed the Weighted Compact Schemes for the simulation of compressible flows in the presence of shock waves. We investigate both analytically and numerically the boundedness of symmetric CFV schemes, which are shown to be quite prone to develop wiggles on coarse grids. The compact filtering procedure by Lele [7] proves effective in damping such unphysical oscillations, allowing for solutions of remarkable accuracy even on very coarse grids. This approach has been applied also by Smirnov et al. [19] in the framework of compact finite-volume methods.

For a given order of accuracy, compact schemes can be *tuned* to achieve spectral-like resolution [7]. We develop and test spectral-like schemes for both interpolation and differentiation; they are derived following a procedure proposed by Lele [7], and optimized by Kim and Lee [24] and by Kobayashi [25].

Although most of the illustrated developments can be extended to boundary-fitted grids, by introducing general coordinate transformations, in this paper the proposed methodology is applied to non-uniform Cartesian grids. We follow the approach based on a coordinate transformation between the physical and the computational space. The alternative strategy, based on direct approximation of the conservation equations in the physical space, was followed by Smirnov et al. [19], and proved effective in dealing with structured non-uniform grids. The motivations for adopting a coordinate transformation are addressed in the paper.

The proposed methodology has been applied to several one- and two-dimensional test cases, both for the scalar transport equation and the Navier–Stokes equations. The one-dimensional tests regard both purely advective and purely diffusive problems, and provide simple indications about the type of problems, which could greatly benefit of the good resolution properties of CFV schemes. The two-dimensional, purely advective scalar transport equation is solved for two standard configurations, the advection of a step discontinuity by a velocity inclined with respect to the computational grid, and the advection of a cone around a circular path. These simulations are particularly revealing of the accuracy and resolution characteristics of the CFV schemes. The good resolution properties are confirmed by the ability of reproducing sharp discontinuities, like a step and sharp cone in the distribution of a scalar field. In addition, the appearence of weak unphysical oscillations confirms the expected fact that symmetric CFV schemes need some special treatment in order to keep under control aliasing errors. This issue has been confirmed in the simulation of the lid-driven cavity. As long as the Reynolds number equals 1000, no special treatment is required in order to obtain a stable simulation, free of wiggles; when the Reynolds number is increased up to 5000, the average kinetic energy increases, until the simulation blows up. It is shown that the application of a high-order compact filter to the advective term is sufficient, in the reported flow configurations, to obtain stable simulations. In order to test the capability of the proposed CFV method to reproduce unsteady phenomena, we have simulated the natural convection flow of a perfectly conductive fluid in a rectangular cavity, with adiabatic horizontal walls, and vertical walls kept at constant, different temperatures. The accuracy of the proposed algorithm has been checked by comparing the numerical against the analytical solution, for the flow configuration of decaying Taylor–Green vortices, showing that sixth-order accuracy is achieved.

The results of this study are encouraging: the proposed high-order CFV approach on staggered grids combines a number of advantages like high resolution, flexibility in implementing different boundary conditions and the possibility to be applied, effectively and accurately, to non-uniform grids.

2. The advection–diffusion equation

In order to introduce the main features of CFV schemes, in this section we address the solution of the two-dimensional, incompressible advection–diffusion transport equation for a passive scalar

$$\frac{\partial \varphi}{\partial t} + \nabla \cdot (\mathbf{u}\varphi) = \frac{1}{Pe}\nabla^2 \varphi, \tag{1}$$

where Pe is the Péclet number. By adopting the Runge–Kutta time-stepping scheme by Le and Moin [20], Eq. (1) can be cast in semi-discrete form

$$\varphi^{(k+1)} - \varphi^{(k)} + \Delta t\left[\gamma^{(k)}\mathscr{H}^{(k)} + \zeta^{(k)}\mathscr{H}^{(k-1)}\right] = \alpha^{(k)}\Delta t\left[\mathscr{D}^{(k+1)} + \mathscr{D}^{(k)}\right], \tag{2}$$

where

$$\mathscr{H}^{(k)} = \nabla \cdot (\mathbf{u}\varphi)^{(k)} = \frac{\partial}{\partial x}(u\varphi)^{(k)} + \frac{\partial}{\partial y}(v\varphi)^{(k)},$$

$$\mathscr{D}^{(k)} = \frac{1}{Pe}\nabla^2\varphi^{(k)} = \frac{1}{Pe}\left[\frac{\partial^2\varphi^{(k)}}{\partial x^2} + \frac{\partial^2\varphi^{(k)}}{\partial y^2}\right].$$

The index k refers to the present Runge–Kutta substep: $k = 1, 2, 3$, with $k = 0$ and $k = 3$ representing the current and the next time steps, respectively. The coefficients $\alpha^{(k)}$, $\gamma^{(k)}$, $\zeta^{(k)}$ are listed in Table 1.

In Eq. (2) the two coordinate directions are still coupled by the diffusive term $\mathscr{D}^{(k+1)}$. The Alternate Direction Implicit approach [17] is adopted in order to render the solution process independent along each coordinate direction, within each Runge–Kutta substep

$$\varphi^{(k+1,h+1)} - \varphi^{(k)} + \Delta t\left(\gamma^{(k)}\mathscr{H}^{(k)} + \zeta^{(k)}\mathscr{H}^{(k-1)}\right) = \alpha^{(k)}\Delta t\left(\mathscr{D}_x^{(k+1,h+1)} + \mathscr{D}_y^{(k+1,h)} + \mathscr{D}^{(k)}\right) \tag{3}$$

followed by

$$\varphi^{(k+1,h+2)} - \varphi^{(k)} + \Delta t\left(\gamma^{(k)}\mathscr{H}^{(k)} + \zeta^{(k)}\mathscr{H}^{(k-1)}\right) = \alpha^{(k)}\Delta t\left(\mathscr{D}_x^{(k+1,h+1)} + \mathscr{D}_y^{(k+1,h+2)} + \mathscr{D}^{(k)}\right). \tag{4}$$

At each time-step, three Runge–Kutta substeps are performed; due to the implicit treatment of the diffusive term each substep requires internal iterations, represented in (3) and (4) by the iteration counter h.

In finite-volume methods Eqs. (3) and (4) are integrated over a control volume; whenever possible, the volume integrals are then modified according to the Gauss' theorem:

$$\int_{c.v.} \mathscr{H}\, \mathrm{d}V = \int_{c.v.} \nabla \cdot (\mathbf{u}\varphi)\, \mathrm{d}V = \int_S \varphi\mathbf{u} \cdot \boldsymbol{n}\, \mathrm{d}S, \tag{5}$$

Table 1
Coefficients for the Runge–Kutta time-stepping scheme [20]

$\alpha^1 = 4/15$	$\alpha^2 = 1/15$	$\alpha^3 = 1/6$
$\gamma^1 = 8/15$	$\gamma^2 = 5/12$	$\gamma^3 = 3/4$
$\zeta^1 = 0$	$\zeta^2 = -17/60$	$\zeta^3 = -5/12$

$$\int_{c.v.} \mathscr{D}\,\mathrm{d}V = \frac{1}{Pe}\int_{c.v.} \nabla^2\varphi\,\mathrm{d}V = \frac{1}{Pe}\int_S \nabla\varphi\cdot\boldsymbol{n}\,\mathrm{d}S. \tag{6}$$

The resulting equations are discretized on a staggered grid, sketched in Fig. 1. A coordinate transformation relates the physical with the computational space in such a way that, in general, the image of the centroid of a computational cell is not located in the centroid of the corresponding physical cell. Nevertheless, we will always refer to it as *cell centre*. With reference to Fig. 1, we define the following quantities in the computational space:

$$\overline{\varphi}^{\xi\eta}_{i,j} = \frac{1}{\Delta\xi_i\Delta\eta_j}\int_{\eta_{j-1/2}}^{\eta_{j+1/2}}\int_{\xi_{i-1/2}}^{\xi_{i+1/2}} \varphi(\xi,\eta)\,\mathrm{d}\xi\,\mathrm{d}\eta, \tag{7}$$

$$\overline{\varphi}^{\eta}_{i+1/2,j} = \frac{1}{\Delta\eta_j}\int_{\eta_{j-1/2}}^{\eta_{j+1/2}} \varphi\left(\xi_{i+1/2},\eta\right)\mathrm{d}\eta, \tag{8}$$

$$\overline{\varphi}^{\xi}_{i,j+1/2} = \frac{1}{\Delta\xi_i}\int_{\xi_{i-1/2}}^{\xi_{i+1/2}} \varphi\left(\xi,\eta_{j+1/2}\right)\mathrm{d}\xi, \tag{9}$$

$$\overline{\frac{\partial\varphi}{\partial\xi}}^{\eta}_{i+1/2,j} = \frac{1}{\Delta\eta_j}\int_{\eta_{j-1/2}}^{\eta_{j+1/2}} \frac{\partial\varphi}{\partial\xi}\left(\xi_{i+1/2},\eta\right)\mathrm{d}\eta, \tag{10}$$

$$\overline{\frac{\partial\varphi}{\partial\eta}}^{\xi}_{i,j+1/2} = \frac{1}{\Delta\xi_i}\int_{\xi_{i-1/2}}^{\xi_{i+1/2}} \frac{\partial\varphi}{\partial\eta}\left(\xi,\eta_{j+1/2}\right)\mathrm{d}\xi. \tag{11}$$

Corresponding quantities are defined in the physical space; in this case, the integrals extend over, and are scaled by, the physical cell width. The advective and diffusive fluxes (7)–(11) are approximated by compact differentiation and interpolation formulas.

We assume the average values of φ onto each computational control volume as main unknowns. The point values, defined at the cell centres, are recovered once and for all at the end of the simulation by a

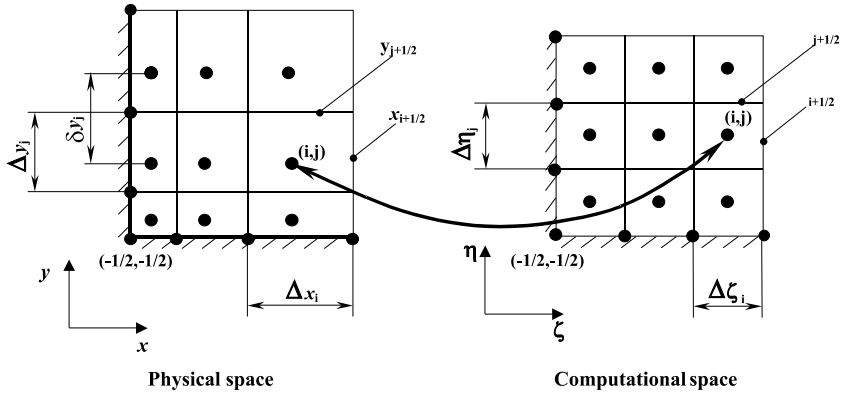

Fig. 1. Geometrical quantities used for the description of a non-uniform Cartesian grid.

deconvolution procedure [18]. This approach seems very natural, in that it recognizes that fluxes and cell-averaged quantities are the basic variables arising from a finite-volume discretization.

2.1. Compact approximation of fluxes

The diffusive fluxes along the ξ direction, Eq. (10), are approximated to fourth-order accuracy by the following symmetric compact equation, valid for uniform Cartesian grids:

$$a_1\overline{\frac{\partial\varphi}{\partial\xi}}^{\eta}_{i+3/2,j}+\overline{\frac{\partial\varphi}{\partial\xi}}^{\eta}_{i+1/2,j}+a_1\overline{\frac{\partial\varphi}{\partial\xi}}^{\eta}_{i-1/2,j}=\frac{a_2}{\Delta\xi}\left(\overline{\varphi}^{\xi\eta}_{i+1,j}-\overline{\varphi}^{\xi\eta}_{i,j}\right). \tag{12}$$

The unknown parameters a_1, a_2 are evaluated by comparing the truncated Taylor series on each side of (12)

$$a_1=\frac{1}{10},\quad a_2=\frac{6}{5}.$$

All the compact approximations presented in this paper have been derived with a similar approach, and the coefficients are listed in Table 2. Whereas Eq. (12) is still applicable near the boundaries when Neumann boundary conditions are enforced on φ, a fourth-order asymmetric formula is required near the Dirichlet boundaries. At the left boundary a fourth-order compact approximation reads

$$\overline{\frac{\partial\varphi}{\partial\xi}}^{\eta}_{i-1/2,j}+a_3\overline{\frac{\partial\varphi}{\partial\xi}}^{\eta}_{i+1/2,j}+a_4\overline{\frac{\partial\varphi}{\partial\xi}}^{\eta}_{i+3/2,j}=\frac{1}{\Delta\xi}\left(a_5\overline{\varphi}^{\eta}_{i-1/2,j}+a_6\overline{\varphi}^{\xi\eta}_{i,j}+a_7\overline{\varphi}^{\xi\eta}_{i+1,j}+a_8\overline{\varphi}^{\xi\eta}_{i+2,j}\right). \tag{13}$$

The variable $\overline{\varphi}^{\eta}_{i-1/2,j}$ represents the assigned face-averaged value on the left boundary. On the right boundary, the specular version of (13) can be used.

The evaluation of the advective fluxes requires interpolation formulas, relating the cell face variables $\overline{\varphi}^{\eta}_{i+1/2,j}$ to the main unknowns $\overline{\varphi}^{\xi\eta}_{i,j}$. A symmetric, fourth-order compact interpolation scheme can be devised as

$$a_9\overline{\varphi}^{\eta}_{i-1/2,j}+\overline{\varphi}^{\eta}_{i+1/2,j}+a_9\overline{\varphi}^{\eta}_{i+3/2,j}=a_{10}\left(\overline{\varphi}^{\xi\eta}_{i,j}+\overline{\varphi}^{\xi\eta}_{i+1,j}\right). \tag{14}$$

Table 2
List of coefficients for the compact equations derived in the paper

$a_1=1/10$	$a_2=6/5$	$a_3=52$	$a_4=23/2$
$a_5=35/2$	$a_6=-1033/12$	$a_7=767/12$	$a_8=14/3$
$a_9=1/4$	$a_{10}=3/4$	$a_{11}=4/3$	$a_{12}=1/6$
$a_{13}=-1/6$	$a_{14}=23/12$	$a_{15}=7/12$	$a_{16}=9/62$
$a_{17}=17/186$	$a_{18}=103/93$	$a_{19}=73/557$	$a_{20}=-69/2785$
$a_{21}=13/3899$	$a_{22}=-3568/19495$	$a_{23}=720/557$	$a_{24}=-120/367$
$a_{25}=-7/367$	$a_{26}=17/367$	$a_{27}=391/367$	$a_{28}=-151/367$
$a_{29}=1/22$	$a_{30}=12/11$	$a_{31}=15$	$a_{32}=-16/15$
$a_{33}=-15$	$a_{34}=50/3$	$a_{35}=-3/5$	$a_{36}=1/6$
$a_{37}=2/3$	$a_{38}=9/11$	$a_{39}=-3/11$	$a_{40}=18/11$
$a_{41}=2/11$	$a_{42}=1/48$	$a_{43}=11/38$	$a_{44}=137/114$
$a_{45}=85/228$	$a_{46}=-23/228$	$a_{47}=1/57$	$a_{48}=1/2$
$a_{49}=1/20$	$a_{50}=527/600$	$a_{51}=17/100$	$a_{52}=-1/600$
$a_{53}=10/21$	$a_{54}=5/126$	$a_{55}=5/6$	$a_{56}=5/28$
$a_{57}=1/252$	$a_{58}=334/899$	$a_{59}=43/1798$	$a_{60}=14335/16182$
$a_{61}=2375/8091$	$a_{62}=79/16182$	$a_{63}=96850/288529$	$a_{64}=9675/577058$
$a_{65}=1297462/4327935$	$a_{66}=69049/8655870$	$a_{67}=1571529/1442645$	

Eq. (14) can be applied near Dirichlet boundaries as well. A fifth-order compact interpolation formula, to be applied close to Neumann boundaries, is

$$\overline{\varphi}^{\eta}_{i-1/2,j} + a_{11}\overline{\varphi}^{\eta}_{i+1/2,j} + a_{12}\overline{\varphi}^{\eta}_{i+3/2,j} = a_{13}\Delta\xi\overline{\frac{\partial\varphi}{\partial\xi}}^{\eta}_{i-1/2,j} + a_{14}\overline{\varphi}^{\xi\eta}_{i,j} + a_{15}\overline{\varphi}^{\xi\eta}_{i+1,j}. \tag{15}$$

2.2. Deconvolution

At the end of the simulation, we recover the point values $\varphi_{i,j}$ from the cell-averaged values $\overline{\varphi}^{\xi\eta}_{i,j}$ by a deconvolution procedure. In the one-dimensional case, a sixth-order deconvolution scheme is

$$a_{16}\varphi_{i+1} + \varphi_i + a_{16}\varphi_{i-1} = a_{17}\overline{\varphi}^{\xi}_{i+1} + a_{18}\overline{\varphi}^{\xi}_{i} + a_{17}\overline{\varphi}^{\xi}_{i-1}, \tag{16}$$

$$\varphi_i + a_{19}\varphi_{i+1} + a_{20}\varphi_{i+2} + a_{21}\varphi_{i+3} = a_{22}\varphi_{i-1/2} + a_{23}\overline{\varphi}^{\xi}_{i}, \tag{17}$$

$$\varphi_i + a_{24}\varphi_{i+1} + a_{25}\varphi_{i+2} = a_{26}\frac{\partial\varphi}{\partial\xi}_{i-1/2}\Delta x + a_{27}\overline{\varphi}^{\xi}_{i} + a_{28}\overline{\varphi}^{\xi}_{i+1}. \tag{18}$$

Eq. (16) can be used in the domain interior; Eqs. (17) and (18) are used near the Dirichlet and the Neumann boundaries, respectively. Two- and three-dimensional deconvolutions can be performed by repeated application of (16)–(18) along each coordinate direction, when ADI or similar methods are adopted.

2.3. Simultaneous solution of physical and compact equations

Semi-implicit time-stepping schemes provide for an implicit treatment of the diffusive term; thus, the compact differentiation equations have to be solved *simultaneously* with the discrete transport equations, leading to an algebraic linear system with $2N$ unknowns, being N the number of control volumes along each coordinate direction. In order to minimize the bandwidth of the resulting coefficient matrix, the equations are sorted cell-wise: for each $i = 1, \ldots, N$, two equations are considered: the first is the physical equation associated with the ith cell; the second is the compact equation for the diffusive flux across the $i + 1/2$ cell face. The unknowns are arranged consequently: first $\overline{\varphi}^{\xi}_{i}$, then $\overline{\partial\varphi}^{\eta}/\partial\xi_{i+1/2}$. This convention leads to a penta-diagonal coefficient matrix, except for the first and last few rows, which can include more terms due to the use of asymmetric compact equations near the boundaries. The resulting algebraic linear system can be efficiently solved by the method described in Appendix B. Two- and three-dimensional unsteady advection–diffusion equations are reduced to a sequence of one-dimensional problems by the ADI or similar techniques [17].

2.4. von Neumann analysis of CFV methods

In this section, we investigate the resolution capability of various spatial-discretization schemes by means of the von Neumann analysis. We address independently diffusion and advection-dominated equations.

The one-dimensional, unsteady diffusion problem with periodic boundary conditions reads

$$\begin{cases} \frac{\partial\varphi}{\partial t} = \Gamma\frac{\partial^2\varphi}{\partial x^2}, & \Gamma > 0, \\ \varphi(x,t) = \varphi(x+L,t) & \forall x \end{cases} \tag{19}$$

A Fourier wave is assumed as initial condition

$$\varphi(x,0) = \mathrm{e}^{2\pi \mathrm{i} k x/L}, \quad k \in \mathscr{N}. \tag{20}$$

The analytical solution of (19) and (20) can be readily obtained as

$$\varphi(x,t) = \mathrm{e}^{-4\pi^2 k^2 \Gamma t/L^2} \mathrm{e}^{2\pi \mathrm{i} k x/L}. \tag{21}$$

We introduce semi-discrete approximations of (19) and (20), in that the time integration is performed analytically. The computational grid is uniform, with N cells covering the interval $[0, L]$. In order to cast the problem (19) in a suitable form for finite-volume discretization, we first integrate over the generic control volume

$$\left.\frac{\partial \overline{\varphi}^x}{\partial t}\right|_j \Delta x = \Gamma \left(\left.\frac{\partial \varphi}{\partial x}\right|_{j+1/2} - \left.\frac{\partial \varphi}{\partial x}\right|_{j-1/2} \right). \tag{22}$$

The unknown quantity in Eq. (22) is the CV-averaged value $\overline{\varphi}^x_j$, which is subject to periodic boundary conditions. Eq. (22) can be cast in matrix form as

$$\frac{\partial \overline{\boldsymbol{\varphi}}^x_\bullet}{\partial t} = \frac{\Gamma}{\Delta x} \mathbf{A} \left.\frac{\partial \boldsymbol{\varphi}}{\partial x}\right|_{\bullet+1/2}, \tag{23}$$

where

$$\overline{\boldsymbol{\varphi}}^x_\bullet = \begin{Bmatrix} \overline{\varphi}^x_1 \\ \overline{\varphi}^x_2 \\ \vdots \\ \overline{\varphi}^x_N \end{Bmatrix}, \quad \left.\frac{\partial \boldsymbol{\varphi}}{\partial x}\right|_{\bullet+1/2} = \begin{Bmatrix} \left.\frac{\partial \varphi}{\partial x}\right|_{3/2} \\ \left.\frac{\partial \varphi}{\partial x}\right|_{5/2} \\ \vdots \\ \left.\frac{\partial \varphi}{\partial x}\right|_{N+1/2} \end{Bmatrix}, \quad \mathbf{A} = \begin{bmatrix} 1 & & & & -1 \\ -1 & 1 & & & \\ \cdots & & & & \\ & & -1 & 1 & \\ & & & -1 & 1 \end{bmatrix} \in \mathscr{M}^{N\times N},$$

where $\mathscr{M}^{N\times N}$ indicates the space of an $N \times N$ real matrices. A suitable initial condition for (23) is obtained by averaging (20) on each control volume

$$\overline{\varphi}^x_j(t=0) = \frac{1}{\Delta x} \int_{(j-1/2)\Delta x}^{(j+1/2)\Delta x} \mathrm{e}^{2\pi \mathrm{i} k x/L} \, \mathrm{d}x = \frac{\sin k\pi/N}{k\pi/N} \mathrm{e}^{2\pi \mathrm{i} j k/N}. \tag{24}$$

The exact cell-averaged solution at time t is

$$\overline{\varphi}^x_j(t) = \mathrm{e}^{-4\pi^2 k^2 \Gamma t/L^2} \frac{\sin k\pi/N}{k\pi/N} \mathrm{e}^{2\pi \mathrm{i} j k/N}. \tag{25}$$

A spatial-discretization scheme for the x-derivative provides a linear relation between $\partial\boldsymbol{\varphi}/\partial x_{\bullet+1/2}$ and $\overline{\boldsymbol{\varphi}}^x_\bullet$, which can be expressed in matrix form as

$$\mathbf{D} \frac{\partial \boldsymbol{\varphi}}{\partial x}_{\bullet+1/2} = \frac{1}{\Delta x} \mathbf{B} \overline{\boldsymbol{\varphi}}^x_\bullet, \quad \mathbf{D}, \mathbf{B} \in \mathscr{M}^{N\times N}. \tag{26}$$

We compare the standard second-order (ST2) with the fourth-order CFV method presented in Section 2 (CS4); the coefficient matrices **D** and **B** assume a general form

$$\mathbf{D} = \begin{bmatrix} 1 & a & & & & & & a \\ a & 1 & a & & & & & \\ \cdots & \cdots & \cdots & \cdots & \cdots & \cdots & \cdots & \cdots \\ \cdots & \cdots & \cdots & \cdots & \cdots & \cdots & \cdots & \cdots \\ \cdots & \cdots & \cdots & \cdots & \cdots & \cdots & \cdots & \cdots \\ \cdots & \cdots & \cdots & \cdots & \cdots & \cdots & \cdots & \cdots \\ & & & & a & 1 & a & \\ a & & & & & & a & 1 \end{bmatrix},$$

$$\mathbf{B} = b \begin{bmatrix} -1 & 1 & & & & & & \\ & -1 & 1 & & & & & \\ \cdots & \cdots & \cdots & \cdots & \cdots & \cdots & \cdots & \cdots \\ \cdots & \cdots & \cdots & \cdots & \cdots & \cdots & \cdots & \cdots \\ \cdots & \cdots & \cdots & \cdots & \cdots & \cdots & \cdots & \cdots \\ \cdots & \cdots & \cdots & \cdots & \cdots & \cdots & \cdots & \cdots \\ & & & & & & -1 & 1 \\ 1 & & & & & & & -1 \end{bmatrix}.$$

The coefficients a and b are

Scheme	a	b
ST2	0	1
CS4	$1/10$	$6/5$

As could have been expected, due to the imposition of periodic boundary conditions, **D** and **B** are circulant matrices [26]. Matrix **D** can be inverted to get $\mathbf{D}^{-1}$; Eq. (23) is rewritten as

$$\frac{\partial \overline{\boldsymbol{\varphi}}^{x}_{\bullet}}{\partial t} = \frac{\Gamma}{(\Delta x)^2} \mathbf{A}\mathbf{D}^{-1}\mathbf{B}\overline{\boldsymbol{\varphi}}^{x}_{\bullet}. \tag{27}$$

The eigenvalues of a tridiagonal, circulant matrix are [26]

$$\lambda^{(k)} = \beta + (\alpha+\gamma)\cos\left(\frac{2k\pi}{N}\right) - \mathrm{i}(\alpha-\gamma)\sin\left(\frac{2k\pi}{N}\right), \quad k = 0,\ldots,N-1,$$

where α, β and γ are the subdiagonal, diagonal and superdiagonal terms, respectively. Thus

$$\begin{aligned} \lambda^{(k)}_{\mathbf{A}} &= 1 - \mathrm{e}^{-2\pi\mathrm{i}k/N}, \\ \lambda^{(k)}_{\mathbf{D}} &= 1 + 2a\cos\left(\frac{2k\pi}{N}\right), \\ \lambda^{(k)}_{\mathbf{B}} &= b\left(-1 + \mathrm{e}^{2\pi\mathrm{i}k/N}\right). \end{aligned} \tag{28}$$

The eigenvalues of $\mathbf{A}\mathbf{D}^{-1}\mathbf{B}$ are thus

$$\lambda^{(k)}_{\mathbf{A}\mathbf{D}^{-1}\mathbf{B}} = F(k) = \frac{\lambda^{(k)}_{\mathbf{A}}\lambda^{(k)}_{\mathbf{B}}}{\lambda^{(k)}_{\mathbf{D}}} = -4b\frac{\sin^2(k\pi/N)}{1+2a\cos(2k\pi/N)}. \tag{29}$$

The eigenvectors of an $N \times N$ circulant matrix are independent of the actual coefficients

$$\boldsymbol{\psi}^{(k)} = \left\{\psi_j^{(k)}\right\} = \left\{\mathrm{e}^{2\pi \mathrm{i} jk/N}\right\}, \quad j,k = 0,\ldots,N-1. \tag{30}$$

By taking into account the initial condition (24), and observing that the eigenvectors (30) form a basis, the solution of (27) can be readily obtained as

$$\overline{\varphi}_j^x(t) = \frac{\sin(k\pi/N)}{k\pi/N}\mathrm{e}^{F(k)\frac{\Gamma t}{\Delta x^2}}\mathrm{e}^{2\pi \mathrm{i} kj/N}. \tag{31}$$

By comparing (31) with (25), it turns out that the ratio

$$H(k) = -F(k)/(4\pi^2 k^2/N^2)$$

represents a suitable measure of the error introduced by the spatial discretization, since it equals unity for the exact solution. By introducing the modified wavenumber $\widetilde{k} = 2k\pi/N = 2k\pi\Delta x/L$, the function $H(\widetilde{k})$ reads

$$H\left(\widetilde{k}\right) = 4b\frac{\sin^2\left(\widetilde{k}/2\right)}{\widetilde{k}^2\left(1+2a\cos\left(\widetilde{k}\right)\right)}, \quad \widetilde{k} \in [0,\pi]. \tag{32}$$

The error functions $1 - H(\widetilde{k})$, obtained by the ST2 and CS4 schemes, are compared in Fig. 2. It is evident that they share the common behavior of reducing the effective diffusivity; that is, the damping of the initial solution is slower than expected. The CS4 behaves much better than the ST2 scheme on the whole wavenumber range.

In Fig. 3 we compare the absolute error, derived by the von Neumann analysis, for both the CS4 and the ST2 schemes as functions of the dimensionless wavenumber $k\Delta x$ and the Fourier number $Fo = \Gamma t/\Delta x^2$. It can be observed that, where Fo is very large, the error is negligibly small at all wavenumbers, for both approaches. Only for small values of Fo the ST2 scheme behaves considerably worse than the CS4 scheme and affects a wider range of wavenumbers.

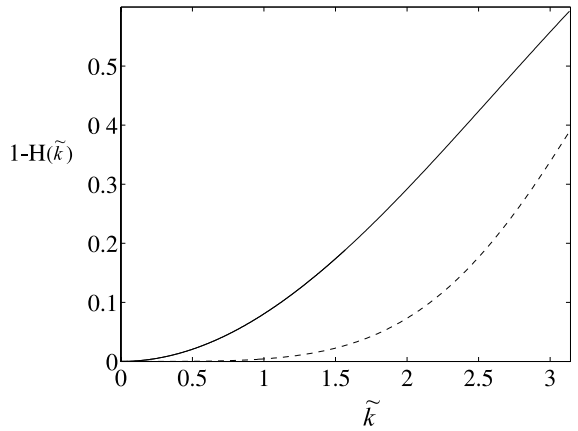

Fig. 2. Error function for two different spatial-discretization schemes considered in Section 2.4 for the diffusion equation. Solid line: ST2; dashed line: CS4.

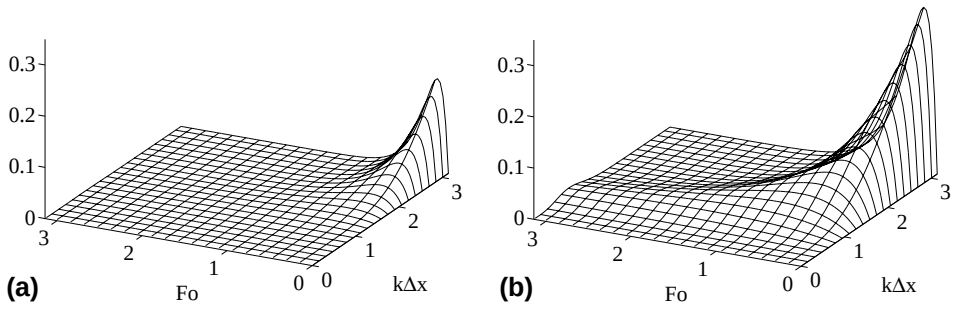

Fig. 3. Absolute error as a function of $k\Delta x$ and $Fo = \Gamma t/\Delta x^2$: (a) CS4; (b) ST2.

As a numerical test, we solved Eq. (19) by imposing the initial condition

$$\varphi(x,0) = 1 - \cos(2\pi x), \quad x \in [0,1]. \tag{33}$$

This function can be developed as a sine-series, so that components of all wavenumbers are present in the final solution. The general analytical solution can be expressed as

$$\varphi(x,t) = \sum_{n=0}^{\infty} A_n \mathrm{e}^{-\frac{(2n+1)^2\pi^2 t}{Pe}} \sin[(2n+1)\pi x], \tag{34}$$

where

$$A_n = \frac{8(-1)^{2n+1} - 1}{(2n+1)\pi\left[(2n+1)^2 - 4\right]}. \tag{35}$$

The comparison with the exact solution, not reported here, confirms the anti-diffusive character of the considered schemes. The behavior of the CS4 scheme is not very different from that of the simpler ST2 scheme. Of course, the error is much smaller, as reported in Table 3. However, the physical phenomenon is correctly reproduced by both methods. This is not surprising, since the largest resolution errors affect the highest wavenumber components, which are more rapidly damped in diffusion-dominated transport phenomena.

The ability of compact schemes to accurately resolve a wider range of wavenumbers becomes more evident in the simulation of advection-dominated phenomena. We focus on the one-dimensional linear advection equation, subject to periodic boundary conditions; a Fourier wave is assumed as initial condition

$$\begin{cases} \frac{\partial\varphi}{\partial t} + c\frac{\partial\varphi}{\partial x} = 0, \\ \varphi(x+L) = \varphi(x), \\ \varphi(x,0) = \mathrm{e}^{2\pi i k x/L}. \end{cases} \tag{36}$$

Table 3
Maximum and rms errors for the diffusion of the initial solution, given by Eq. (33), on a uniform grid with 32 control volumes

Scheme	Max error	rms Error
ST2	2.17×10^{-3}	1.23×10^{-3}
CS4	2.67×10^{-5}	1.56×10^{-5}

The diffusion equation reads $\partial_t\varphi = \partial_{x,x}\varphi$, which implies that the length-scale corresponds to the domain dimension L, while the time is rendered non-dimensional as $\alpha t/L^2$, being α the diffusion coefficient. The solution is advanced until the non-dimensional time $t = 0.1$.

The analytical solution of (36) is

$$\varphi_j(t) = \mathrm{e}^{2\pi \mathrm{i} k\left(x_j - ct\right)/L}. \tag{37}$$

The initial solution is transported in the positive x-direction by the advection velocity c. By similar arguments as adopted for the 1D diffusion equation, it can be shown that the semi-discrete solution of (36) can be expressed by

$$\widetilde{\varphi}_j(t) = \mathrm{e}^{2\pi \mathrm{i} k\left(x_j - c_\mathrm{e} t\right)/L}, \tag{38}$$

where c_e is the *effective* advection velocity. By comparing (37) with (38) it turns out that the ratio of the effective to the exact advection velocity can be expressed as a function of $\widetilde{k} = 2k\pi\Delta x/L$

$$\frac{c_\mathrm{e}}{c} = \frac{2a\sin\left(\widetilde{k}\right)}{\left[1 + 2\alpha\cos\left(\widetilde{k}\right)\right]\widetilde{k}}. \tag{39}$$

As for the CS4 scheme, the coefficients a and α in (39) correspond to the coefficients a_9 and a_{10} in the compact interpolation equation (14) used to evaluate the advective fluxes, which is rewritten here for convenience

$$\alpha\varphi_{i+3/2} + \varphi_{i+1/2} + \alpha\varphi_{i-1/2} = a\left(\overline{\varphi}^x_{i+1} + \overline{\varphi}^x_i\right).$$

Values corresponding to the ST2 and CS4 schemes are as follows:

Scheme	a	α
ST2	1/2	0
CS4	3/4	1/4

The velocity ratio (39), which accounts for the dispersion errors, has been evaluated for the ST2 and CS4 schemes and is plotted in Fig. 4. It is evident that the reduction of the advection velocity, characteristic of symmetric spatial-discretization schemes [27], is modest for the CS4 scheme in a wide range of wave-numbers.

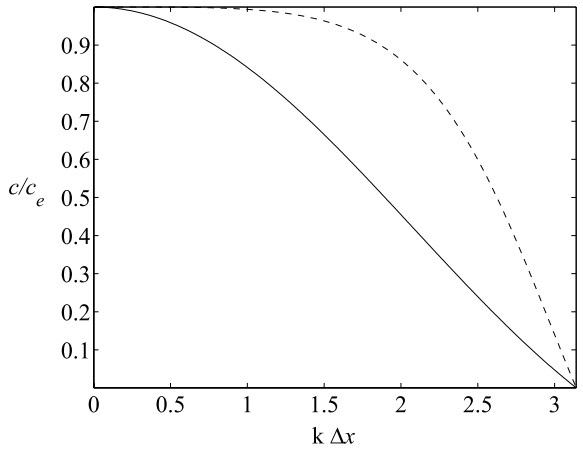

Fig. 4. Dispersion error represented by the ratio of the effective versus the exact advection velocity. Dashed line: CS4; solid line: ST2.

3. Two-dimensional momentum equations

In this section, we present a CFV discretization of the Navier–Stokes equations for two-dimensional, incompressible flows with constant properties, on a staggered, Cartesian non-uniform grid. The procedure derives directly from that used for the advection–diffusion equation, reported in Section 2. Additional complications have to be faced, concerning the placement and approximation of velocity components on a staggered grid, the derivation of suitable approximations for pressure and the solution of a Poisson's equation, arising in the fractional-step procedure [28].

While both fourth- and sixth-order algorithms have been developed and tested, in this section we present only sixth-order schemes, with the objective of showing that CFV methods of order higher than fourth can be achieved.

3.1. Temporal discretization and fractional-step algorithm

The non-dimensional continuity and momentum equations, in Cartesian coordinates, read

$$\nabla \cdot \mathbf{u} = 0, \tag{40}$$

$$\frac{\partial \mathbf{u}}{\partial t} + \nabla \cdot (\mathbf{u}\mathbf{u}) + \nabla p = \frac{1}{Re}\nabla^2 \mathbf{u} + \mathbf{f}. \tag{41}$$

By using a semi-implicit time-stepping scheme, in conjunction with the Projection 2 fractional-step algorithm by Gresho [28], the following set of semi-discrete equations is obtained:

$$\mathbf{u}^* - \mathbf{u}^n + \frac{\Delta t}{2}\left[3\nabla \cdot (\mathbf{u}\mathbf{u})^n - \nabla \cdot (\mathbf{u}\mathbf{u})^{n-1}\right] + \Delta t \nabla p^n = \frac{\Delta t}{2Re}\left[\nabla^2 \mathbf{u}^* + \nabla^2 \mathbf{u}^n\right] + \Delta t \mathbf{F}^{n+1}, \tag{42}$$

$$\nabla^2 \phi = \nabla \cdot \mathbf{u}^*, \tag{43}$$

$$\mathbf{u}^{n+1} = \mathbf{u}^* - \nabla \phi, \tag{44}$$

$$p^{n+1} = p^n + \frac{2\phi}{\Delta t}. \tag{45}$$

The explicit Adams–Bashforth scheme is used for the advective term, while the implicit Crank–Nicolson discretization is applied to the diffusive term. The provisional velocity $\mathbf{u}^*$ does not respect continuity, and is corrected in the projection step (44) in order to return the divergence-free velocity $\mathbf{u}^{n+1}$. The scalar field ϕ is usually addressed as *pseudo-pressure*, and is used both to enforce continuity in (44) and to obtain a first-order accurate estimate for the pressure field at the new time-step in (45).

3.2. Spatial discretization of the provisional momentum equations

Eq. (42) is solved for the provisional velocity components $\overline{u}^{\xi\eta}_{i+1/2,j}$ and $\overline{v}^{\xi\eta}_{i,j+1/2}$, averaged over suitable control volumes in the computational space. The discretization process involves also face-averaged values, like $\overline{u}^{\eta}_{i,j}$, $\overline{v}^{\xi}_{i,j}$, $\overline{p}^{\eta}_{i,j}$ and $\overline{p}^{\xi}_{i,j}$. The asterisk in $\mathbf{u}^*$, indicating provisional velocity components, will be dropped out for notational convenience. In the staggered grid arrangement by Harlow and Welch [14] the control volume for each velocity component is shifted along the corresponding coordinate direction. All scalar variables, like pressure and pseudo-pressure, are associated with main control volumes. Fig. 5 helps in

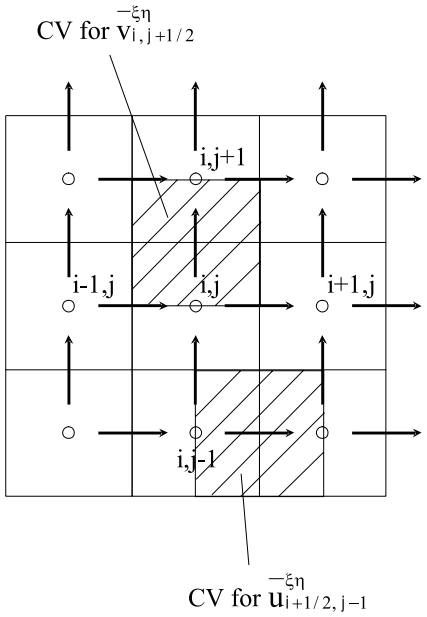

Fig. 5. Arrangement of variables on a staggered grid.

locating all variables on the computational plane. In the following sections, we address separately the spatial discretization of each term in (42).

3.2.1. Transient term

In the CFV method, the *transient* terms, namely $\mathbf{u}$ or $\mathbf{u}^n$, have to be averaged over a CV. With reference to the u component, the averaging process is carried out as follows:

$$\frac{1}{\Delta V_u}\int\int_{\Delta V_u} u\,\mathrm{d}V = \frac{1}{\Delta\Omega_u}\int\int_{\Delta\Omega_u} u\,\det(\mathbf{J})\,\mathrm{d}\xi\,\mathrm{d}\eta, \tag{46}$$

where ΔV_u indicates a physical control volume, shifted along the coordinate direction x, corresponding to the computational control volume $\Delta\Omega_u$. The Jacobian matrix $\mathbf{J}$ is defined as

$$\mathbf{J} = \begin{pmatrix} \frac{\partial x}{\partial \xi} & \frac{\partial x}{\partial \eta} \\ \frac{\partial y}{\partial \xi} & \frac{\partial y}{\partial \eta} \end{pmatrix}. \tag{47}$$

The *metrics*, i.e. the elements of the Jacobian matrix $\mathbf{J}$, can be evaluated either analytically or numerically; in this work we used an analytical calculation. Since we focus on Cartesian grids, the above expressions simplify as follows:

$$x = x(\xi), \quad y = y(\eta), \quad \mathbf{J} = \begin{pmatrix} \frac{\mathrm{d}x}{\mathrm{d}\xi} & 0 \\ 0 & \frac{\mathrm{d}y}{\mathrm{d}\eta} \end{pmatrix}, \quad \det(\mathbf{J}) = \frac{\mathrm{d}x}{\mathrm{d}\xi}\frac{\mathrm{d}y}{\mathrm{d}\eta}. \tag{48}$$

For the numerical evaluation of Eq. (46) we devised a sixth-order, 2D integration scheme, which does not rely on the simplifications (48)

$$\overline{fg}_{i,j}^{\Delta\Omega} = \frac{1}{\Delta\Omega}\int\int_{\Delta\Omega} fg\,\mathrm{d}\xi\,\mathrm{d}\eta \approx \overline{f}_{i,j}^{\Delta\Omega}\overline{g}_{i,j}^{\Delta\Omega} + a_{42}\left[\left(\overline{f}_{i+1,j}^{\Delta\Omega} - \overline{f}_{i-1,j}^{\Delta\Omega}\right)\left(\overline{g}_{i+1,j}^{\Delta\Omega} - \overline{g}_{i-1,j}^{\Delta\Omega}\right) + \left(\overline{f}_{i,j+1}^{\Delta\Omega} - \overline{f}_{i,j-1}^{\Delta\Omega}\right)\left(\overline{g}_{i,j+1}^{\Delta\Omega} - \overline{g}_{i,j-1}^{\Delta\Omega}\right)\right], \tag{49}$$

where f and g represent generic functions/variables. Asymmetric equations, involving more terms, were derived for the calculations near non-periodic boundaries.

The CV-average of $\det(\mathbf{J})$ can be evaluated in the computational space by Eq. (49), which involves the cell-averaged metrics. In the case of Cartesian grids, these quantities can be evaluated directly as

$$\overline{\frac{\mathrm{d}x}{\mathrm{d}\xi}}^{\Delta\Omega_u} = \frac{1}{\Delta\xi\,\Delta\eta}\int_{\xi_i}^{\xi_{i+1}}\int_{\eta_{j-1/2}}^{\eta_{j+1/2}}\frac{\mathrm{d}x}{\mathrm{d}\xi}\,\mathrm{d}\xi\,\mathrm{d}\eta = \frac{x_{i+1}-x_i}{\Delta\xi},$$

$$\overline{\frac{\mathrm{d}y}{\mathrm{d}\eta}}^{\Delta\Omega_u} = \frac{y_{j+1/2}-y_{j-1/2}}{\Delta\eta}.$$

Thus we substitute in Eq. (49), shifted half cell right

$$\overline{g}_{i+1/2,j}^{\Delta\Omega_u} = \overline{\det(\mathbf{J})}^{\Delta\Omega_u} = \frac{1}{\Delta\xi\,\Delta\eta}(x_{i+1}-x_i)\left(y_{j+1/2}-y_{j-1/2}\right),$$

$$\overline{f}_{i+1/2,j}^{\Delta\Omega_u} = \overline{u}_{i+1/2,j}^{\Delta\Omega_u}.$$

Even though Eq. (49) leads only to linear terms in $\overline{u^*}^{\Delta\Omega_u}$, we adopted a simpler, second-order accurate in time, deferred-correction approach

$$\overline{u}_{i+1/2,j}^{\Delta V_u} = \overline{u}_{i+1/2,j}^{\Delta\Omega_u} + \left\{\left[2\left(\overline{u}_{i+1/2,j}^{\Delta V_u}\right)^n - \left(\overline{u}_{i+1/2,j}^{\Delta V_u}\right)^{n-1}\right] - \left[2\left(\overline{u}_{i+1/2,j}^{\Delta\Omega_u}\right)^n - \left(\overline{u}_{i+1/2,j}^{\Delta\Omega_u}\right)^{n-1}\right] + \mathrm{O}\left[(\Delta t)^2\right]\right\}. \tag{50}$$

The u-momentum equation is solved for the provisional velocity $\overline{u}_{i+1/2,j}^{\Delta\Omega_u}$, while all the remaining terms in brackets contribute to the right-hand side.

It is worth remarking that Eq. (49) is a particular case of the more general approximation problem

$$\overline{fgh}^{\Delta\Omega} = \frac{1}{\Delta\Omega}\int\int_{\Delta\Omega} fgh\,\mathrm{d}\Omega \approx \mathscr{L}\left(\overline{f}_{\bullet}^{\Delta\Omega}\overline{g}_{\bullet}^{\Delta\Omega}\overline{h}_{\bullet}^{\Delta\Omega}\right), \tag{51}$$

where $\mathscr{L}$ indicates linear combination of suitable cell-averaged quantities, while $\overline{f}_{\bullet}^{\Delta\Omega}\overline{g}_{\bullet}^{\Delta\Omega}\overline{h}_{\bullet}^{\Delta\Omega}$ represents the generic product of CV-averaged quantities. The averages can be taken over different CVs. Eq. (51) can be interpreted as the problem of approximating integrals of a product of two functions

$$\overline{fgh}^{\Delta\Omega} = \overline{f(gh)}^{\Delta\Omega} \approx \mathscr{L}\left(\overline{f}_{\bullet}^{\Delta\Omega}\overline{gh}_{\bullet}^{\Delta\Omega}\right), \quad \overline{gh}^{\Delta\Omega} \approx \mathscr{L}\left(\overline{g}_{\bullet}^{\Delta\Omega}\overline{h}_{\bullet}^{\Delta\Omega}\right). \tag{52}$$

3.2.2. Advective terms

We present the discretization procedure for the advective terms in the x-momentum equation. Application to the other direction is straightforward. Integration of the advective terms in Eq. (42) over a physical control volume leads to

$$\int\int_{\Delta V_u}\nabla\cdot(u\mathbf{u})\,\mathrm{d}V = \int_{\Delta S_u} u\mathbf{u}\cdot\mathbf{n}\,\mathrm{d}S. \tag{53}$$

For 2D Cartesian grids, introducing the geographical notation for convenience

$$\int_{\Delta S_u} u\mathbf{u}\cdot\mathbf{n}\,\mathrm{d}S = \int_{\Delta S_u^{\mathrm{e}}} uu\,\mathrm{d}y - \int_{\Delta S_u^{\mathrm{w}}} uu\,\mathrm{d}y + \int_{\Delta S_u^{\mathrm{n}}} uv\,\mathrm{d}x - \int_{\Delta S_u^{\mathrm{s}}} uv\,\mathrm{d}x, \tag{54}$$

where ΔS_u^{e}, ΔS_u^{w}, ΔS_u^{n}, ΔS_u^{s} indicate the *east*, *west*, *north* and *south* faces of the control volume, respectively. By introducing the coordinate transformation, Eq. (54) can be cast as follows:

$$\int_{\Delta S_u} u\mathbf{u}\cdot\mathbf{n}\,\mathrm{d}S = \int_{\Delta S_u^{\mathrm{e}}} uu\frac{\mathrm{d}y}{\mathrm{d}\eta}\,\mathrm{d}\eta - \int_{\Delta S_u^{\mathrm{w}}} uu\frac{\mathrm{d}y}{\mathrm{d}\eta}\,\mathrm{d}\eta + \int_{\Delta S_u^{\mathrm{n}}} uv\frac{\mathrm{d}x}{\mathrm{d}\xi}\,\mathrm{d}\xi - \int_{\Delta S_u^{\mathrm{s}}} uv\frac{\mathrm{d}x}{\mathrm{d}\xi}\,\mathrm{d}\xi. \tag{55}$$

Each integral in (55) is evaluated by repeated application of compact, 1D averaging schemes. A sixth-order scheme for averaging along η, applicable to internal control volumes, reads

$$\begin{aligned}\overline{fg}^{\eta}_j + a_{43}\left(\overline{fg}^{\eta}_{j+1} + \overline{fg}^{\eta}_{j-1}\right) = {} & a_{44}\overline{f}^{\eta}_j\overline{g}^{\eta}_j + a_{45}\left(\overline{f}^{\eta}_{j+1}\overline{g}^{\eta}_{j+1} + \overline{f}^{\eta}_{j-1}\overline{g}^{\eta}_{j-1}\right) + a_{46}\left(\overline{f}^{\eta}_{j+1}\overline{g}^{\eta}_j + \overline{f}^{\eta}_j\overline{g}^{\eta}_{j+1} + \overline{f}^{\eta}_{j-1}\overline{g}^{\eta}_j + \overline{f}^{\eta}_j\overline{g}^{\eta}_{j-1}\right)\\ & + a_{47}\left(\overline{f}^{\eta}_{j+1}\overline{g}^{\eta}_{j-1} + \overline{f}^{\eta}_{j-1}\overline{g}^{\eta}_{j+1}\right).\end{aligned} \tag{56}$$

The approximation of terms containing uu in (55) requires the evaluation of the quantities $\overline{u}^{\eta}_{i,\bullet}$ at the centre of the main control volumes; for this purpose we use the following compact interpolation scheme:

$$\begin{aligned}a_{49}\overline{u}^{\eta}_{i-2,j} + a_{48}\overline{u}^{\eta}_{i-1,j} + \overline{u}^{\eta}_{i,j} + a_{48}\overline{u}^{\eta}_{i+1,j} + a_{49}\overline{u}^{\eta}_{i+2,j} = {} & a_{50}\left(\overline{u}^{\xi\eta}_{i+1/2,j} + \overline{u}^{\xi\eta}_{i-1/2,j}\right) + a_{51}\left(\overline{u}^{\xi\eta}_{i+3/2,j} + \overline{u}^{\xi\eta}_{i-3/2,j}\right)\\ & + a_{52}\left(\overline{u}^{\xi\eta}_{i+5/2,j} + \overline{u}^{\xi\eta}_{i-5/2,j}\right).\end{aligned} \tag{57}$$

The calculation of the advective terms involving the mixed product uv requires some interpolation before Eq. (56) can be applied. Indeed, both terms $\overline{u}^{\xi}_{i+1/2,j+1/2}$ and $\overline{v}^{\xi}_{i+1/2,j+1/2}$ must be evaluated. The face-averaged velocity $\overline{u}^{\xi}_{i+1/2,j+1/2}$ is obtained by applying Eq. (57) along η

$$\begin{aligned}&a_{49}\overline{u}^{\xi}_{i+1/2,j-3/2} + a_{48}\overline{u}^{\xi}_{i+1/2,j-1/2} + \overline{u}^{\xi}_{i+1/2,j+1/2} + a_{48}\overline{u}^{\xi}_{i+1/2,j+3/2} + a_{49}\overline{u}^{\xi}_{i+1/2,j+5/2}\\ &\quad = a_{50}\left(\overline{u}^{\xi\eta}_{i+1/2,j} + \overline{u}^{\xi\eta}_{i+1/2,j+1}\right) + a_{51}\left(\overline{u}^{\xi\eta}_{i+1/2,j-1} + \overline{u}^{\xi\eta}_{i+1/2,j+2}\right) + a_{52}\left(\overline{u}^{\xi\eta}_{i+1/2,j-2} + \overline{u}^{\xi\eta}_{i+1/2,j+3}\right)\end{aligned} \tag{58}$$

the term $\overline{v}^{\xi}_{i+1/2,j+1/2}$ is obtained by compact interpolation along ξ

$$\begin{aligned}&a_{54}\overline{v}^{\xi}_{i+5/2,j+1/2} + a_{53}\overline{v}^{\xi}_{i+3/2,j+1/2} + \overline{v}^{\xi}_{i+1/2,j+1/2} + a_{53}\overline{v}^{\xi}_{i-1/2,j+1/2} + a_{54}\overline{v}^{\xi}_{i-3/2,j+1/2}\\ &\quad = a_{55}\left(\overline{v}^{\xi}_{i+1,j+1/2} + \overline{v}^{\xi}_{i,j+1/2}\right) + a_{56}\left(\overline{v}^{\xi}_{i+2,j+1/2} + \overline{v}^{\xi}_{i-1,j+1/2}\right) + a_{57}\left(\overline{v}^{\xi}_{i+3,j+1/2} + \overline{v}^{\xi}_{i-2,j+1/2}\right).\end{aligned} \tag{59}$$

3.2.3. Diffusive terms

With reference to the diffusive terms in the u-momentum equation, integration over a staggered CV leads to

$$\int_{\Delta S_u} \frac{\partial u}{\partial n}\,\mathrm{d}S = \int_{\Delta S_u^{\mathrm{e}}} \frac{\partial u}{\partial n}\,\mathrm{d}S - \int_{\Delta S_u^{\mathrm{w}}} \frac{\partial u}{\partial n}\,\mathrm{d}S + \int_{\Delta S_u^{\mathrm{n}}} \frac{\partial u}{\partial n}\,\mathrm{d}S - \int_{\Delta S_u^{\mathrm{s}}} \frac{\partial u}{\partial n}\,\mathrm{d}S. \tag{60}$$

By introducing the coordinate transformation and referring to Cartesian grids

$$\int_{\Delta S_u^{\mathrm{e}}} \frac{\partial u}{\partial \xi}\frac{\mathrm{d}\xi}{\mathrm{d}x}\frac{\mathrm{d}y}{\mathrm{d}\eta}\,\mathrm{d}\eta - \int_{\Delta S_u^{\mathrm{w}}} \frac{\partial u}{\partial \xi}\frac{\mathrm{d}\xi}{\mathrm{d}x}\frac{\mathrm{d}y}{\mathrm{d}\eta}\,\mathrm{d}\eta + \int_{\Delta S_u^{\mathrm{n}}} \frac{\partial u}{\partial \eta}\frac{\mathrm{d}\eta}{\mathrm{d}y}\frac{\mathrm{d}x}{\mathrm{d}\xi}\,\mathrm{d}\xi - \int_{\Delta S_u^{\mathrm{s}}} \frac{\partial u}{\partial \eta}\frac{\mathrm{d}\eta}{\mathrm{d}y}\frac{\mathrm{d}x}{\mathrm{d}\xi}\,\mathrm{d}\xi.$$

We present the approximation of the integral on ΔS_u^{e}, the others being treated similarly. Since $x = x(\xi)$ for Cartesian grids, it turns out that

$$\int_{\Delta S_u^e} \frac{\partial u}{\partial \xi}\frac{\mathrm{d}\xi}{\mathrm{d}x}\frac{\mathrm{d}y}{\mathrm{d}\eta}\,\mathrm{d}\eta = \left.\frac{\mathrm{d}\xi}{\mathrm{d}x}\right|_{i+1}\int_{\Delta S_u^e}\frac{\partial u}{\partial \xi}\frac{\mathrm{d}y}{\mathrm{d}\eta}\,\mathrm{d}\eta, \tag{61}$$

where the index $i+1$ states that ΔS_u^e is the *east* face of a staggered CV along ξ. The integral on the right-hand side in (61) can be approximated by the compact averaging scheme (56), *moving* along η, provided that the terms $\overline{\partial u}^{\eta}/\partial\xi_{i+1/2,\bullet}$ have been previously evaluated. The differentiation is carried out by a compact differentiation scheme

$$\begin{aligned} &a_{59}\frac{\overline{\partial u}^{\eta}}{\partial\xi_{i-2,j}} + a_{58}\frac{\overline{\partial u}^{\eta}}{\partial\xi_{i-1,j}} + \frac{\overline{\partial u}^{\eta}}{\partial\xi_{i,j}} + a_{58}\frac{\overline{\partial u}^{\eta}}{\partial\xi_{i+1,j}} + a_{59}\frac{\overline{\partial u}^{\eta}}{\partial\xi_{i+2,j}} \\ &\quad = \frac{a_{60}}{\Delta\xi}\left[\overline{u}^{\xi\eta}_{i+1/2,j} - \overline{u}^{\xi\eta}_{i-1/2,j}\right] + \frac{a_{61}}{\Delta\xi}\left[\overline{u}^{\xi\eta}_{i+3/2,j} - \overline{u}^{\xi\eta}_{i-3/2,j}\right] + \frac{a_{62}}{\Delta\xi}\left[\overline{u}^{\xi\eta}_{i+5/2,j} - \overline{u}^{\xi\eta}_{i-5/2,j}\right]. \end{aligned} \tag{62}$$

Asymmetric equations were derived for the calculations near the boundaries.

3.2.4. Pressure terms

The pressure forces, acting on the faces of a staggered CV, have to be approximated by using the available pressure variables, that is $\overline{p}^{\xi\eta}_{i,j}$. Presenting the fractional-step method, it will be shown that a second-order approximation could suffice

$$\overline{p}^{x}_{i,j} \approx \overline{p}^{\xi\eta}_{i,j} \approx \overline{p}^{y}_{i,j}. \tag{63}$$

We derived also a compact high-order scheme

$$\overline{p}^{y}_{i,j} = \frac{1}{\Delta y_j}\int_{y_{j+1/2}}^{y_{j-1/2}} p\,\mathrm{d}y = \frac{1}{\Delta y_j}\int_{\eta_{j+1/2}}^{\eta_{j-1/2}} p\frac{\mathrm{d}y}{\mathrm{d}\eta}\,\mathrm{d}\eta. \tag{64}$$

As in the evaluation of previous integrals of products, we use Eq. (56) in order to approximate the last integral in Eq. (64). Before doing that, we need an approximation for $\overline{p}^{\eta}_{i,\bullet}$ at the centre of the collocated CVs, which is obtained by a compact deconvolution scheme

$$a_{64}\overline{p}^{\eta}_{i+2,j} + a_{63}\overline{p}^{\eta}_{i+1,j} + \overline{p}^{\eta}_{i,j} + a_{63}\overline{p}^{\eta}_{i-1,j} + a_{64}\overline{p}^{\eta}_{i-2,j} = a_{65}\left(\overline{p}^{\xi\eta}_{i+1,j} + \overline{p}^{\xi\eta}_{i-1,j}\right) + a_{66}\left(\overline{p}^{\xi\eta}_{i+2,j} + \overline{p}^{\xi\eta}_{i-2,j}\right) + a_{67}\overline{p}^{\xi\eta}_{i,j}. \tag{65}$$

Asymmetric equations, as usual, were derived near the boundaries.

3.3. Fractional-step method and continuity equation

As mentioned before, the fractional-step algorithm by Gresho [28] leads to a Poisson's equation for the pseudo-pressure, which allows to *project* the provisional velocity field $\mathbf{u}^*$ into a divergence-free velocity field $\mathbf{u}^{n+1}$, which is a better approximation of the true velocity field at the new time step. The projection step is performed just once on each time step, leading to a second-order time-accurate velocity field [28]. The correction term $\nabla\phi$ is of order $(\Delta t)^2$; thus, if Eqs. (43) and (44) were discretized in space with second-order accuracy, the additional error introduced by the fractional-step method would be of order $(\Delta t)^2(\Delta x)^2$, and thus would not degrade excessively the accuracy of the whole method. By repeating iteratively the projection step within each time step, the provisional velocity field will eventually satisfy both the discrete momentum and continuity equations [29]; then, when using iteratively the fractional-step method, it is sufficient to discretize the term $\nabla\cdot\mathbf{u}^*$ with high spatial accuracy, in order to derive a highly accurate projected velocity field $\mathbf{u}^{n+1}$.

The left-hand side in Poisson's equation is thus discretized by a standard second-order method

$$\int_{\Delta S} \frac{\partial \phi}{\partial n}\, \mathrm{d}S = \int_{\Delta S} \mathbf{u}^* \cdot \mathbf{n}\, \mathrm{d}S, \tag{66}$$

$$\int_{\Delta S} \frac{\partial \phi}{\partial n}\, \mathrm{d}S \approx \left(\frac{\phi_{i+1,j} - \phi_{i,j}}{\delta x_i} - \frac{\phi_{i,j} - \phi_{i-1,j}}{\delta x_{i-1}} \right) \Delta y_j + \left(\frac{\phi_{i,j+1} - \phi_{i,j}}{\delta y_j} - \frac{\phi_{i,j} - \phi_{i,j-1}}{\delta y_{j-1}} \right) \Delta x_i.$$

The right-hand side can be expressed exactly as

$$\left(\overline{u}^y_{i+1/2,j} - \overline{u}^y_{i-1/2,j} \right) \Delta y_j + \left(\overline{v}^x_{i,j+1/2} - \overline{v}^x_{i,j-1/2} \right) \Delta x_i. \tag{67}$$

The face-averaged velocities in (67) are evaluated in the transformed plane

$$\overline{u}^y_{i+1/2,j} = \frac{1}{\Delta y_j} \int_{y_{j-1/2}}^{y_{j+1/2}} u\, \mathrm{d}y = \frac{1}{\Delta y_j} \int_{\eta_{j-1/2}}^{\eta_{j+1/2}} u \frac{\mathrm{d}y}{\mathrm{d}\eta}\, \mathrm{d}\eta. \tag{68}$$

The integral averaging in (68) is performed by using (56). The compact deconvolution (65) is used to approximate $\overline{u}^{\eta}_{\bullet+1/2,j}$ from $\overline{u}^{\xi\eta}_{\bullet+1/2,j}$.

The discrete Poisson's equation is then solved by a Matrix-Decomposition method [30], and values for $\overline{\phi}^{xy}$ are obtained. The corrected velocity field is obtained by the discrete version of (43) as

$$\overline{u}^y_{i+1/2,j} = \overline{u^*}^y_{i+1/2,j} - \frac{\phi_{i+1,j} - \phi_{i,j}}{\delta x_i}, \quad \overline{v}^x_{i,j+1/2} = \overline{v^*}^x_{i,j+1/2} - \frac{\phi_{i,j+1} - \phi_{i,j}}{\delta y_j}.$$

It is worth mentioning that, after the correction step (44), we are left with corrected values of, say, $\overline{u}^y_{i+1/2,j}$. In order to recover $\overline{u}^{\eta}_{i+1/2,j}$ we invert the integral averaging Eq. (56). In addition, after evaluating $\overline{u}^{\eta}_{i+1/2,j}$ and, similarly, $\overline{v}^{\xi}_{i,j+1/2}$, we need to derive the corrected values for $\overline{u}^{\xi\eta}_{i+1/2,j}$ and $\overline{v}^{\xi\eta}_{i,j+1/2}$, which were assumed as *main* unknowns. To this end, we invert the compact deconvolution (65).

The pressure field is updated by (45)

$$\overline{p}^{\xi\eta}_{i,j} \approx \overline{p^*}^{\xi\eta}_{i,j} - 2\frac{\overline{\phi}^{xy}_{i,j}}{\Delta t}. \tag{69}$$

By iterating the fractional step, the pressure field is enforced toward the unique solution, allowing the velocity field to satisfy both the momentum and the continuity equations, to high-order spatial accuracy. In this limit, even the pressure field is solved with high-order accuracy.

3.4. Deconvolution

At the end of the simulation, the point-values of the velocity components are recovered by recursive application of the compact deconvolution (65), along both coordinate directions.

3.5. Further characteristics of the proposed methodology

3.5.1. About the use of staggered grids

The staggered grid arrangement was introduced mainly with the aim of avoiding pressure–velocity decoupling in second-order finite-volume and finite-difference schemes [14]. This property is conserved by higher-order finite-difference and finite-volume methods on staggered grids [13]. Pereira et al. [18] showed that, based on the eigenvalues of the discrete gradient operator, the velocity and pressure fields are coupled in compact (fourth-order) finite-volume schemes on collocated grids, as long as an odd number of grid-points is used along each coordinate direction, which in fact does not constitute a serious limitation. This

property can be proved analytically for fourth-order schemes on uniform grids and periodic or Dirichlet boundary conditions. However, the strength of the pressure–velocity coupling is still an open issue when generic schemes, geometries and boundary conditions are involved. Nevertheless, the results of several numerical tests, carried out by Pereira et al. [18] and by Smirnov et al. [19] with odd numbers of control volumes along each coordinate direction, do not reveal spurious oscillations related to pressure–velocity decoupling.

Another favorable property of the staggered grid arrangement is the availability of velocity components at locations, where they are needed in the discrete continuity equation; in collocated grid arrangements, these velocity components must be interpolated from quantities defined at the cell centres. Similarly, the pressure is defined where it is needed, in order to represent the pressure force acting on the staggered control volumes for the velocity components and, unlike in collocated schemes [17], the discrete representation of the pressure gradient in the momentum equations does not require extrapolating the pressure field to those portions of the boundary, where Dirichlet boundary conditions are enforced on the velocity field. Despite this favorable properties of the staggered grid arrangement, Sharatchandra and Rhode [31,32] verified that, in some cases, collocated schemes give more accurate results than their staggered equivalents. However, Nagarajan et al. [16] arrived to opposite conclusions, reporting that compact finite-difference schemes on staggered grids are at least as accurate as collocated schemes, but much more robust due to their better conservation properties.

In view of the above discussion, it is a hard task, at present time, stating a priori which approach, and under which respect, is better, either collocated or staggered. Further research should possibly focus on the conservation properties of both methods.

3.5.2. About the use of metrics

Introducing a coordinate transformation, from the physical to a computational domain, is a common practice in finite-difference schemes [11], and it is well known that a careful treatment of metrics is needed, in order avoid a sensible reduction of the quality of the results. In addition, the inadequate representation of metrics can cause relevant conservation errors, which lead to unstable calculations [33]. Finite-volume approximations can be formulated either in physical or in transformed space [34]; the first approach is commonly followed with second-order methods, since it leads to more intuitive formulations and does not require a specific treatment of metrics. Smirnov et al. [19,35] developed a compact finite-volume method working in physical space; they use Cartesian velocity components in a collocated grid arrangement. Results of several simulations show that the method is both stable and accurate. A seeming drawback of the *physical* approach, in the case of high-order methods, consists in the need of developing compact interpolation, differentiation and quadrature formulas directly on the deformed mesh; besides being more complicate, the derivation of such discrete operators requires a larger number of *free* coefficients or, equivalently, of neighboring nodes, in order to reach a given formal order of accuracy, since the truncation error depends on all coordinate directions [19]. This drawback could become even more severe in three dimensions.

In this paper, we introduce a coordinate transformation mainly because, based on the works of other authors, it is reasonable expecting better kinetic energy conservation properties. We recall results by Vasilyev [15], suggesting that grid-independent differentiation and interpolation schemes seem unavoidable in order to extend the conservation properties, valid on uniform grids, to Cartesian non-uniform grids. The validity of this conclusion, demonstrated by Vasilyev [15] in the framework of traditional finite-difference methods on Cartesian grids, is uncertain for CFV methods; nevertheless, it seems reasonable to infer that the symmetries of a numerical method, on which the conservation properties are based upon [15], should be maintained on any grid, which would impose the use of coordinate transformations.

Gamet et al. [36] state that, in the framework of finite-difference schemes, the discretization approach based on metrics (JT) should be rejected, since it is considerably less accurate than the Fully Integrated

Metrics (FIM) method, based on compact differentiation in physical space. However, in our opinion, their arguments are not strikingly conclusive, since they compare the JT and FIM methods by differentiating an analytical function on a *random* grid. A boundary-fitted grid, which would be suitable to be used with compact finite-difference or CFV methods, is usually generated by solving a differential or variational problem [34], so that it will be generally quite smooth. In addition, it is probably unfair to expect that a JT method works on a random grid since, rigorously speaking, the Jacobian of the coordinate transformation cannot be defined, in this case. In Fig. 6, we report the errors obtained in the same test performed by Gamet et al. [36] using both random and smoothly varying grids; it is evident that, even though the FIM approach works better on both random and smooth grids, the improvement with respect to the JT method is negligibly small, if any, on the latter. We used the following grid distributions:

- *Random*

$$x = L[\xi + Ch\eta].$$

- *Smooth*

$$x = L\left[\xi + \frac{C-1}{2\pi}\sin(2\pi\xi)\right],$$

where ξ is the coordinate in the transformed $[0,1]$ interval, $L = 2\pi$, $C = 0.3$ and $\eta \in [-1,1]$ indicates a sequence of random numbers. The function to be differentiated is

$$f(x) = \cos(\omega_0 x + \phi_0)$$

with

$$\omega_0 = 4, \quad \phi_0 = 1.$$

In view of the preceeding discussion, it is evident that there are no clear-cut arguments suggesting which, between the FIM and the JT approaches, works better with CFV schemes: both have advantages and

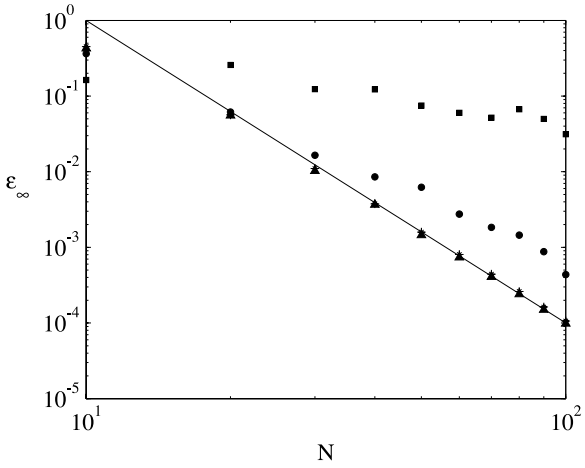

Fig. 6. Numerical differentiation of $f(x)$ by fourth-order compact schemes. Squares: JT, random grid, metrics evaluated by compact schemes; circles: FIM, random grid; triangles: FIM, smooth grid; asterisks: JT, smooth grid, metrics evaluated by compact schemes; plus signs (hidden by the asterisks): JT, smooth grid, metrics evaluated analytically; solid line: fourth-order slope.

drawbacks. The FIM approach allows for an easier and more *physical* derivation of a compact finite-volume method, while the investigations by Morinishi et al. [13], Vasilyev [15], Verstappen and Veldman [37] seem to suggest that the conservation properties of the coordinate-transformation approach are superior.

4. Spectral-like fourth-order compact schemes

Kim and Lee [24] devised a systematic procedure to obtain spectral-like compact schemes, with optimal resolution properties. A least-squares fitting in the wavenumber space is used, in order to optimize the resolution properties of a scheme. The weighting function is selected in such a way that the integral error function can be evaluated explicitly. The spectral-like compact schemes derived in this paper, however, do not present a natural choice for the weighting function. Following the same procedure proposed in [24], we derived integral error functions which could indeed be integrated analytically, but we did not succeed in solving the non-linear system of two equations resulting from the error-minimization requirement, not even with the aid of a symbolic manipulator [38]. Thus, we used numerical quadrature and minimization. Only spectral-like symmetric schemes have been investigated, while near the boundaries we resort to the asymmetric schemes derived for the standard CS4 method.

4.1. Spectral-like compact differentiation

The general equation for a tridiagonal fourth-order, spectral-like compact differentiation scheme in the domain interior is

$$\alpha \frac{\partial \varphi}{\partial x}_{i+3/2} + \frac{\partial \varphi}{\partial x}_{i+1/2} + \alpha \frac{\partial \varphi}{\partial x}_{i-1/2} = \frac{a}{\Delta x}\left(\overline{\varphi}^{x}_{i+1} - \overline{\varphi}^{x}_{i}\right) + \frac{b}{\Delta x}\left(\overline{\varphi}^{x}_{i+2} - \overline{\varphi}^{x}_{i-1}\right). \tag{70}$$

Eq. (70) is written for the one-dimensional case; nevertheless, it can be used in multi-dimensional simulations, by simply averaging each quantity on a cell-width, along the coordinate directions which are not involved in the differentiation process. By Fourier analysis [24] it is easy to derive the following equation for the modified wavenumber, k_e:

$$k_e \Delta x = 2\frac{a \sin\left(\frac{k\Delta x}{2}\right) + b \sin\left(\frac{3k\Delta x}{2}\right)}{1 + 2\alpha \cos\left(k\Delta x\right)} \frac{\sin\left(\frac{k\Delta x}{2}\right)}{\frac{k\Delta x}{2}}. \tag{71}$$

In order to optimize the resolution properties of (70), we impose the following constraint [24]:

$$\begin{aligned} E &= \frac{\int_0^\pi \left(k_e \Delta x - k\Delta x\right)^2 W^2(\epsilon, k\Delta x) d(k\Delta x)}{\int_0^\pi W^2(\epsilon, k\Delta x) d(k\Delta x)}, \\ \nabla E &= 0, \\ W(\epsilon, k\Delta x) &= \left[1 + \epsilon(\cos\left(k\Delta x\right) - 1/2)\right]^2. \end{aligned} \tag{72}$$

That is, we require the minimization of the integral weighted error function E. The parameter ϵ decreases progressively the weight of errors introduced at large wavenumbers, which could otherwise introduce undesired oscillations in the $k_e\Delta x$ profile [24]. By expanding (70) in Taylor series, it is easy to derive the following accuracy constraints:

$$\begin{aligned}
&\text{Order } 0 \qquad 2\alpha - a - 3b + 1 = 0,\\
&\text{Order } 1 \qquad \alpha - \frac{1}{2}a - \frac{3}{2}b + \frac{1}{2} = 0,\\
&\text{Order } 2 \qquad \frac{5}{4}\alpha - \frac{5}{24}a - \frac{13}{8}b + \frac{1}{8} = 0,\\
&\text{Order } 3 \qquad \frac{13}{24}\alpha - \frac{1}{16}a - \frac{11}{16}b + \frac{1}{48} = 0.
\end{aligned} \tag{73}$$

By solving (73) it turns out that

$$\alpha = \frac{6}{5}b + \frac{1}{10}, \quad a = -\frac{3}{5}b + \frac{6}{5}. \tag{74}$$

By substituting (74) into (72), E is made a function of only α_7 and ϵ. The minimization requirement (72) leads to

$$b = 0.105, \quad \epsilon = 0.67. \tag{75}$$

The resulting effective modified wavenumber $k_e\Delta x$ is compared in Fig. 7 with the actual wavenumber $k\Delta x$, and with the modified wavenumber obtained from the second-order, the standard fourth-order compact and the sixth-order tridiagonal compact schemes.

4.2. Spectral-like compact interpolation

A tridiagonal spectral-like fourth-order interpolation scheme reads

$$\alpha\varphi_{i-1/2} + \varphi_{i+1/2} + \alpha\varphi_{i+3/2} = a(\overline{\varphi}^x_i + \overline{\varphi}^x_{i+1}) + b(\overline{\varphi}^x_{i-1} + \overline{\varphi}^x_{i+2}). \tag{76}$$

As remarked in the preceding section, Eq. (76) is written for the one-dimensional case, but can be used also in two or three dimensions. We now consider $\varphi(x)$ as a function that admits a Fourier integral representation

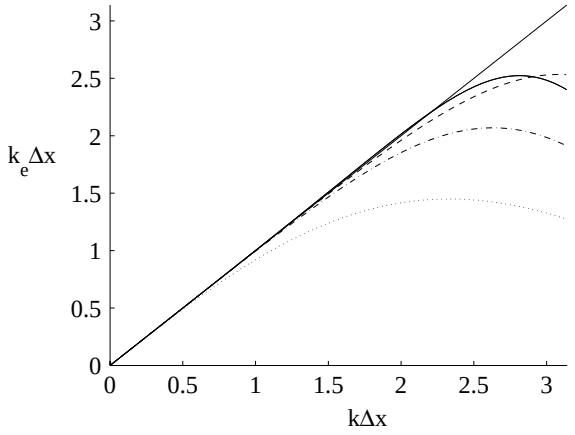

Fig. 7. Effective wavenumber for compact differentiation schemes. Solid straight line: exact differentiation; dotted line: ST2; dash-dotted line: CS4; solid line: OCS4; dashed line: sixth-order symmetric scheme.

$$\Phi(k) = \int_{-\infty}^{\infty} \varphi(x) \frac{e^{-ikx}}{\sqrt{2\pi}}\, dx,$$
$$\varphi(x) = \int_{-\infty}^{\infty} \Phi(k) \frac{e^{ikx}}{\sqrt{2\pi}}\, dk. \tag{77}$$

Thus

$$\varphi(x_{j+1/2}) = \int_{-\infty}^{\infty} \Phi(k) \frac{e^{ikx_{j+1/2}}}{\sqrt{2\pi}}\, dk. \tag{78}$$

In addition, we define a transfer function H as follows:

$$\varphi_{j+1/2} = \int_{-\infty}^{\infty} H(k\Delta x)\Phi(k) \frac{e^{ikx_{j+1/2}}}{\sqrt{2\pi}}\, dk, \tag{79}$$

where $\varphi_{j+1/2}$ is the discrete approximation to $\varphi(x_{j+1/2})$ obtained by Eq. (76). By performing the Fourier transform of Eq. (76) it is easy to show that

$$H(k\Delta x) = 2\frac{a\sin(k\Delta x) + b[\sin(2k\Delta x) - \sin(k\Delta x)]}{k\Delta x[1 + 2\alpha\cos(k\Delta x)]}. \tag{80}$$

The closer is H to unity, the better are the resolution properties of (76). By following the same procedure outlined in Section 4.1 we derived

$$\begin{aligned}
&\text{Order } 0 \quad && 2\alpha - 2a - 2b = -1,\\
&\text{Order } 1 \quad && \alpha - a - b = -1/2,\\
&\text{Order } 2 \quad && \frac{5}{4}\alpha - \frac{7}{12}a - \frac{31}{12}b = -\frac{1}{8},\\
&\text{Order } 3 \quad && \frac{13}{24}\alpha - \frac{5}{24}a - \frac{29}{24}b = -\frac{1}{48},
\end{aligned} \tag{81}$$

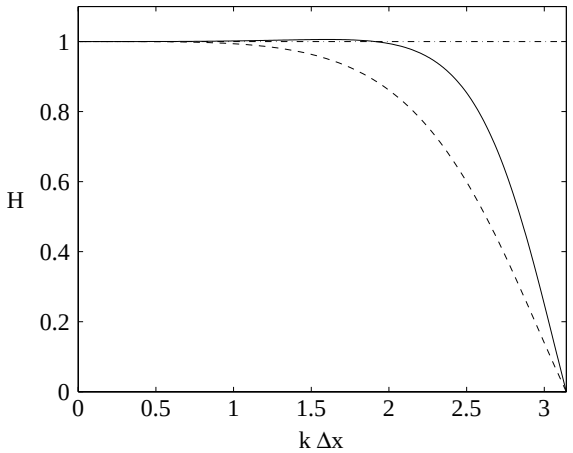

Fig. 8. Transfer function for the optimal-resolution interpolation scheme. The solid line shows the optimized scheme (OCS4) while the dashed line corresponds to the standard fourth-order scheme (CS4).

$$\alpha = 3b + 1/4, \quad a = 2\alpha_{10} + 3/4. \tag{82}$$

At this stage, only b is left unknown. It is set by numerically evaluating the minimum of the following integral error function:

$$E(k\Delta x) = \frac{\int_0^\pi (H-1)^2 W^2 \, \mathrm{d}k\Delta x}{\int_0^\pi W^2 \, \mathrm{d}k\Delta x}. \tag{83}$$

The weighting function W cannot be defined as in (72), since in that case the errors at the highest wavenumbers would still have too much influence, leading to overshooting in the $H(k\Delta x)$ profile. Thus, we tried several weighting functions, all of them vanishing at $k\Delta x = \pi$. Since the results were not strongly dependent on the actual weighting function, we arbitrarily select a simple function $W = 1/2[1 + \cos(k\Delta x)]$. In order to further limit overshooting, we integrated in the range 0–0.7π. By following this procedure we obtained $b = 4/100$. The resulting transfer functions are shown in Fig. 8.

5. Spurious oscillations induced by the spatial discretization

In the presence of a boundary layer the numerical solution is prone to develop spurious cell-to-cell oscillations, known as *wiggles*. Central schemes are particularly affected by this problem, in that they do not introduce any numerical diffusivity [17]. Various expedients are commonly used in order to control the onset of wiggles. Liu and co-workers [23] proposed the Weighted Compact Schemes for the accurate reproduction of flow discontinuities. Lele [7] used compact filters at the end of each time-step in order to damp high-wavenumber oscillations. We tested one of such fourth-order compact filters in the solution of the steady advection–diffusion equation with both the CS4 and the spectral-like scheme, derived in the previous section (OCS4 hereafter), at increasing cell-Péclet number; the ability of such filters to control the onset of wiggles is represented in Fig. 9 for a cell-Péclet number of 2.5. From the same Fig. 9, it is also evident that the filtering limits the magnitude of wiggles. In addition, it is worth remarking that the spectral-like scheme is more prone to develop spurious oscillations than the CS4 scheme.

Patankar [39] studies the onset of wiggles for the one-dimensional, steady advection–diffusion equation. We apply this analysis to the compact schemes derived in this paper, as briefly outlined in the following.

The dimensionless form of the steady, one-dimensional advection–diffusion equation, defined on the interval $[0, 1]$, subject to two Dirichlet boundary conditions, reads

$$\begin{aligned} &\frac{\mathrm{d}\varphi}{\mathrm{d}x} = \frac{1}{Pe}\frac{\mathrm{d}^2\varphi}{\mathrm{d}x^2}, \\ &\varphi(x=0) = 0, \\ &\varphi(x=1) = 1, \end{aligned} \tag{84}$$

where Pe is the Péclet number, based on the whole interval length. A uniform grid is used, with grid spacing Δx. We focus on the region bounded by the nodes $j-1$ and $j+1$, so that $\Delta x = 1/2$ and $Pe = 2P_\mathrm{c}$, being P_c the cell-Péclet number

$$P_\mathrm{c} = \frac{u\Delta x}{\Gamma}. \tag{85}$$

The exact solution of (84) is

$$\varphi(x) = \frac{\mathrm{e}^{2P_\mathrm{c}x} - 1}{\mathrm{e}^{2P_\mathrm{c}} - 1}. \tag{86}$$

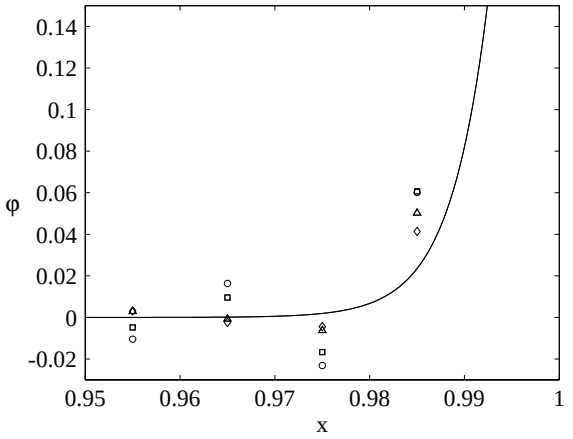

Fig. 9. Boundary layer test for CS4 and optimal schemes. Solid line: exact solution of (84); squares: CS4; triangles: filtered CS4; circles: OCS4; diamonds: filtered OCS4.

We aim to determine the value of φ_j resulting from the selected spatial-discretization schemes. To this end, we first integrate Eq. (84) over the control volume relative to node j, which is bounded by the endpoints $j-1/2$ and $j+1/2$. The resulting algebraic equation reads

$$\varphi_{j+1/2}-\varphi_{j-1/2}=\frac{1}{2P_c}\left[\frac{d\varphi}{dx}_{j+1/2}-\frac{d\varphi}{dx}_{j-1/2}\right]. \tag{87}$$

Eq. (87) can be approximated by an arbitrary spatial-discretization scheme. The advective and diffusive fluxes at the locations $j\pm 1/2$ are evaluated by using compact interpolation and differentiation equations. The remaining quantities are obtained from the exact solution (86). As a result, approximations for φ_j are derived as functions of P_c.

When both the diffusive and the advective fluxes across the control volume faces are obtained from compact approximations, Eqs. (12) and (14), the average value of φ over the jth control volume results in

$$\begin{aligned}\overline{\varphi}_j=&[(2P_c^2-9P_c+12)e^{3P_c}+(9P_c-12)e^{2P_c}+(9P_c+12)\,e^{P_c}-24P_ce^{1/2P_c}-2P_c^2\\&-9P_c-12]e^{-1/2P_c}/[24P_c(e^{2P_c}-1)].\end{aligned} \tag{88}$$

The deconvolution procedure (16) can then be applied in order to recover point values from cell-averaged values, leading to

$$\begin{aligned}\varphi_j=&-[e^{5P_c/2}(324P_c)+e^{3P_c}(-1440-206P_c^2+927P_c)+e^{2P_c}(1440-927P_c)+e^{P_c}(-1440-927P_c)\\&+2556P_ce^{P_c/2}+1440+206P_c^2+927P_c]e^{-P_c/2}/[2232P_c(e^{2P_c-1})].\end{aligned} \tag{89}$$

It can be observed that

$$\lim_{P_c\to+\infty}\varphi_j(P_c)=-\infty,\quad \lim_{P_c\to-\infty}\varphi_j(P_c)=+\infty \tag{90}$$

indicating that the method is not bounded. Similar results can be obtained for the spectral-like scheme derived in Section 4. The exact solution for φ_j is compared with results obtained by the proposed compact schemes in Fig. 10. It is evident that the standard CS4 scheme performs better than the spectral-like, as could have been expected since improved resolution corresponds to a lower filtering of the shorter wavelengths. This feature agrees with the numerical results presented in Fig. 9.

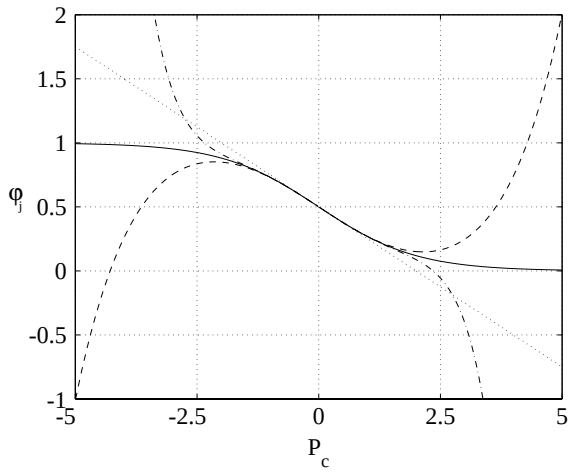

Fig. 10. Comparison of $\varphi_j(P_c)$ profiles for several discretization schemes. Solid line: exact solution; dashed line: CS4 scheme; dash-dotted line: OCS4 scheme, as presented in Section 4; dots: ST2.

6. Results

Simulations have been performed for several one- and two-dimensional flow configurations, for both the scalar transport and the Navier–Stokes equations, by using different spatial-discretization schemes. Our purpose is to verify the following issues:

(1) The solution technique we described for the incompressible Navier–Stokes equations allows to retain the formal order of accuracy of the schemes for the compact interpolation and differentiation. A verification of the formal order of accuracy of the proposed method is performed by comparison with the analytical solution of Taylor–Green vortices. The convergence in simulations more close to those of practical interest is investigated by simulating a lid-driven cavity at $Re = 5000$ on increasingly fine grids.

(2) The proposed method of dealing with non-uniform grids allows to accurately resolve boundary layer regions. In addition, the formal order of accuracy of the method is preserved on non-uniform grids.

(3) Spectral-like CFV methods guarantee improved resolution with respect to CFV schemes of even higher formal accuracy. This issue becomes evident when simulating complex flows on *affordable* grids, while it is evident that, in the limit of very fine grids, the scheme with higher asymptotic accuracy will provide the best results.

(4) As already pointed out by Smirnov et al. [19] and by Nagarajan et al. [16], symmetric compact schemes are highly sensible to aliasing errors. The use of high-order compact filters [7] is verified to effectively eliminate aliasing errors, thus leading to stable simulations. Results of several calculations of the lid-driven cavity at $Re = 5000$ are reported; without filtering applied to the velocity field, the growth of instabilities cannot be controlled, while the simulations performed by filtering the advective term at each time-step are both stable and accurate.

6.1. One-dimensional test cases

In order to compare the resolution characteristics of different spatial-discretization schemes, we simulate the advection of a Gaussian wave from $x = 0.2$ to $x = 0.6$ by a uniform velocity $c = 1.0$. The initial solution is

$$\varphi = \mathrm{e}^{-(x-x_0)^2/\left(2\sigma^2\right)} \tag{91}$$

with $\sigma = 0.01$ and $x_0 = 0.2$. Periodic boundary conditions are assumed, and the CFL number is kept as small as 0.002, so that time-discretization errors can be confidently neglected. We aim to focus on the macroscopic behavior of different spatial-discretization schemes. Several central and upwind schemes are compared in Fig. 11; QUICK and QUICKEST [40] are considered, since they form the basis for several advective schemes. The effective advection velocity c_e obtained by the central discretization schemes is lower than the exact velocity c, with CS4 introducing the smallest error. The CS4 scheme obtains better results than a standard fourth-order scheme, ST4 hereafter, confirming results obtained by the von Neumann analysis [7], which display better resolution properties for compact schemes, compared to traditional methods sharing the same asymptotic order of accuracy. The differences among the various schemes can be better appreciated in Fig. 12, showing the cumulative phase error obtained from the numerical solutions. The cumulative phase error between the Discrete Fourier Transforms of the exact and a computed solution is defined by

$$\epsilon_\vartheta(k\Delta x) = \sum_{h=0}^{k} \left| \widetilde{\vartheta}(h\Delta x) - \vartheta(h\Delta x) \right| \frac{2\pi}{N}, \tag{92}$$

where the tilde indicates the phase angle for the numerical solution. It is evident that the resolution properties of the CS4 scheme are superior in the range of $k\Delta x$ between 0 and 1.25. The error at higher wavenumbers is comparable for all central schemes, as indicated by the parallel slope of all error curves beyond this range. The two upwind methods show a quite peculiar behavior, since they accumulate large phase errors at the small wavenumbers, but give raise to smaller phase errors in the high-wavenumber range, compared to all the central schemes.

The same test case is used in order to investigate the effectiveness of the spectral-like scheme for interpolation. Results obtained on two different grids are shown in Fig. 13. The solution obtained by the spectral-like scheme displays much smaller oscillations than the corresponding solution, obtained by the traditional fourth-order compact method, and the wave is better reproduced.

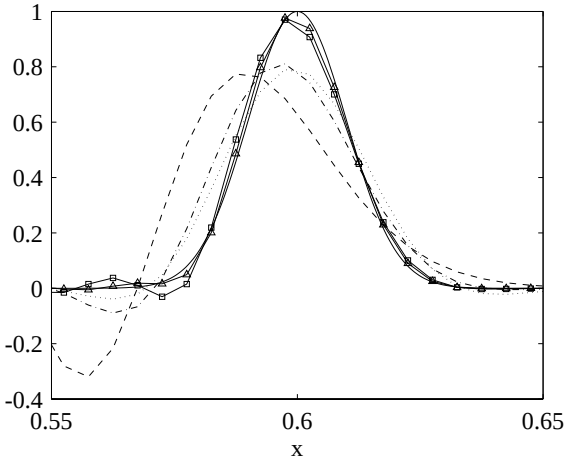

Fig. 11. Gaussian wave advected to its final position. Solid line: exact solution; triangles: CS4; squares: ST4; dashed line: ST2; dash-dotted line: QUICK; dotted line: QUICKEST.

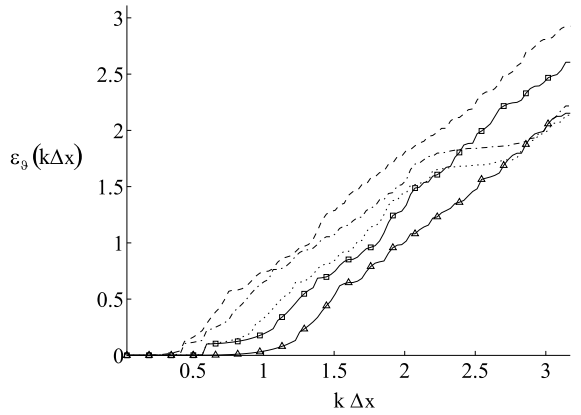

Fig. 12. Cumulative phase error for the advection of a Gaussian wave. Triangles: CS4; squares: ST4; dashed line: ST2; dash-dotted line: QUICK; dotted line: QUICKEST.

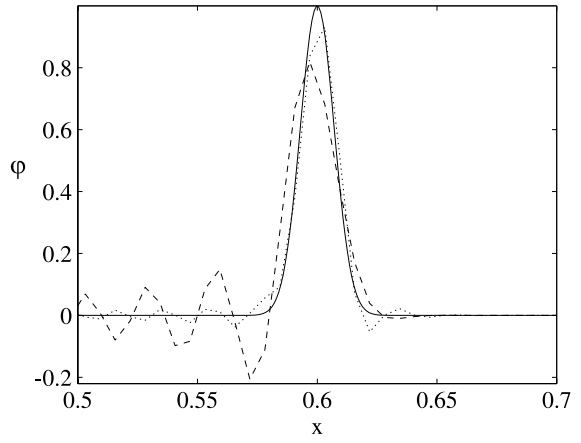

Fig. 13. Advection of a Gaussian wave from $x = 0.2$ to $x = 0.6$, with advection velocity $c = 1.0$. Results obtained by both the CS4 and the OCS4 schemes are compared, on a uniform grid of 160 control volumes. Solid line: analytical solution; dashed line: CS4; dots: OCS4.

6.2. Two-dimensional scalar transport equation

The proposed numerical formulation for multi-dimensional problems is tested by simulating the advection of a sharp cone in a circular path of radius $r_0 = 0.25$, with a rotation period of $\pi/2$. The computational domain is a $[0,1] \times [0,1]$ square, while the base diameter of the cone is 0.1. Homogeneous Dirichlet boundary conditions are imposed. The CS4 scheme is used to simulate one complete revolution of the cone, on a 64×64 uniform grid. Fig. 14 compares the final shape of the cone with corresponding results, obtained by the ST2 scheme on a 128×128 uniform grid. The cone is faithfully reproduced by the CS4 scheme, and the energy propagated into the wake is limited, even on such a coarse grid, which allows for only six control volumes to be enclosed within the base of the cone. On the other hand, the ST2 scheme is neither able to conserve the cone shape, nor to avoid large oscillations in all the computational domain.

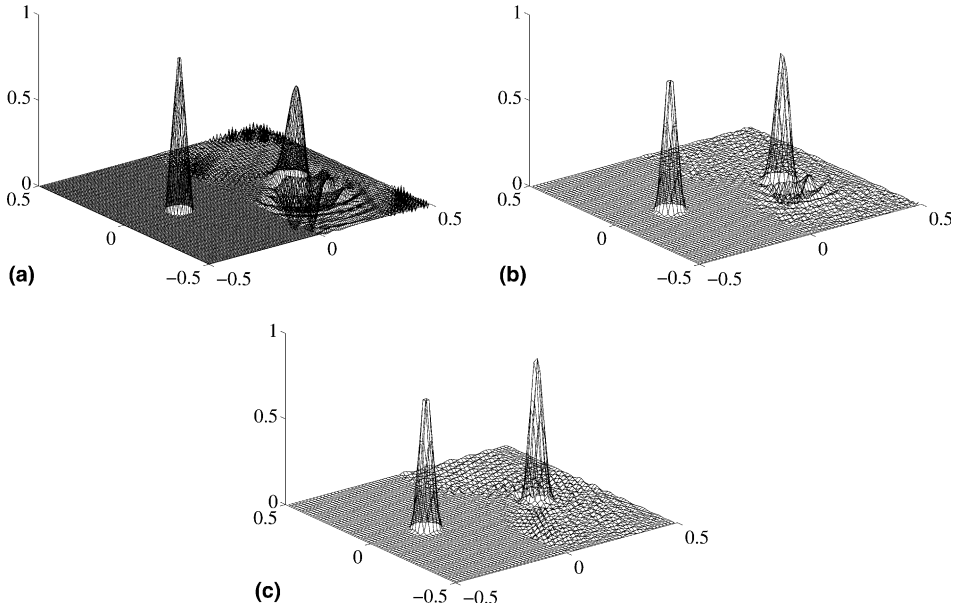

Fig. 14. Final configuration of a sharp cone, advected in a circular path, after a complete revolution: (a) ST2 scheme on a 128×128 uniform grid; (b) CS4 scheme on a 64×64 uniform grid; (c) OCS4 scheme on a 64×64 uniform grid. Dirichlet boundary conditions are enforced.

Results obtained by the spectral-like scheme on a 64×64 uniform grid are shown in Fig. 14(c). The lower intensity of wiggles shows the improved resolution characteristics of such method.

In order to quantify the influence of the CFV representation of boundary conditions, Fig. 15 shows the calculated solution, on a 64×64 uniform grid, with periodic boundary conditions. The wiggles almost disappear, and an unphysical wave persists only in the cone wake, for the CS4 scheme. With the optimal resolution scheme, the intensity of the unphysical wave is strongly damped. By comparing Figs. 14 and 15, it is evident that the use of asymmetric compact schemes near the Dirichlet boundaries does not affect sensibly the results.

Fig. 15(c) shows the final cone shape obtained by a sixth-order CFV method on a 64×64 uniform grid. The fourth-order, spectral-like scheme requires a slightly lower computational effort than the sixth-order compact scheme and the right choice between the two methods depends on the specific application. The von Neumann analysis shows that when better resolution is needed an optimized fourth-order scheme should be chosen. The test of the advection of a sharp cone confirms these theoretical results, being the mean misplacement of the cone after one revolution slightly higher when it is performed, on a relatively coarse 64×64 uniform grid, by the sixth-order compact scheme.

When the flow is inclined with respect to the computational grid, artificial diffusion takes place, with intensity related to the angle of inclination. This effect is well documented [17,27]. In order to access the sensitivity of the proposed compact scheme to the grid orientation, we consider the advection of a stepwise scalar distribution, in the case of zero molecular diffusion. If there were no numerical diffusion, the stepwise distribution would be transported downstream without any distortion. Upwind schemes are known to smear the step-discontinuity, while central schemes produce unphysical oscillations. Both the ST2 and CS4 schemes were used, and results obtained on a 32×32 uniform grid are shown in Fig. 16. In [25] it is observed that compact schemes are much like spectral methods, due to the implicit nature of both discrete operators. This spectral character can be recognized in Fig. 16, where the computed solution overestimates

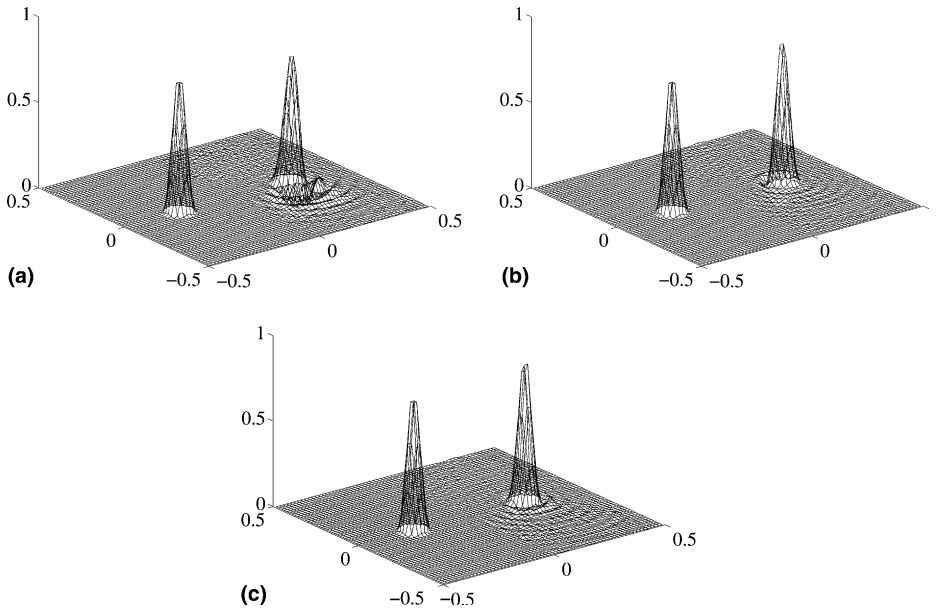

Fig. 15. Final configuration of a sharp cone, advected in a circular path, after a complete revolution: (a) CS4 scheme on a 64×64 uniform grid, with periodic boundary conditions; (b) OCS4 scheme on a 64×64 uniform grid, with periodic boundary conditions; (c) sixth-order CFV scheme on a 64×64 uniform grid with periodic boundary conditions.

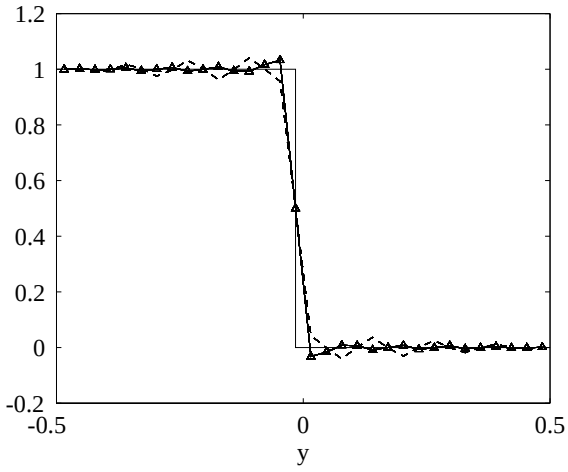

Fig. 16. Advection of a discontinuity. The flow is inclined at 45° with respect to the computational grid. Solid line: exact solution; dashed line: ST2 scheme; triangles: CS4 scheme.

the exact scalar distribution, in a narrow region around the discontinuity, giving raise to a sort of Gibbs' phenomenon. It was verified that the magnitude of the peak does not tend to vanish with increasing grid resolution, although it gets closer to the discontinuity. The unphysical oscillations produced by the CS4 method are much smaller than those obtained by the ST2 scheme, and are highly localized around the discontinuity.

6.3. Two-dimensional laminar Navier–Stokes equations

6.3.1. Simulation of Taylor–Green vortices

The asymptotic order of accuracy of various versions of the proposed CFV method has been determined by simulating the decay of Taylor–Green vortices. This flow configuration admits an analytical solution

$$\begin{aligned} u(x,y,t) &= -\sin(x)\cos(y)\mathrm{e}^{-2\nu t}, \\ v(x,y,t) &= \cos(x)\sin(y)\mathrm{e}^{-2\nu t}, \\ p(x,y,t) &= \frac{1}{4}(\cos(2x)+\cos(2y))\mathrm{e}^{-4\nu t}. \end{aligned} \tag{93}$$

Table 4 reports absolute and rms errors obtained at time $t = 0.05$, with a fixed time step of $\Delta t = 10^{-6}$, which accounts for negligible time-discretization errors. Three sets of results are reported, obtained by using a semi-implicit Crank–Nicolson/Adams–Bashforth fractional-step method. Results A were obtained with a sixth-order CFV code and enforcing Dirichlet boundary conditions, which are imposed according to (93). Results B were obtained with a fourth-order CFV code, using periodic boundary conditions. Results C were obtained with the same method used in case A, except that a non-uniform grid was used. From Table 4 several conclusions can be drawn.

(1) The extension of the proposed CFV methodology to higher than fourth-order accuracy is feasible.
(2) We effectively derived asymmetric, high-order compact schemes for the representation of Dirichlet boundary conditions.
(3) The proposed method for dealing with non-uniform Cartesian grids is effective, and does not affect the asymptotic order of accuracy.
(4) The proposed fractional-step method is accurate, and leads to high-order accurate in space results for both velocity and pressure.

6.4. Two-dimensional lid-driven cavity at $Re = 1000$

The two-dimensional square lid-driven cavity flow at $Re = 1000$ has been extensively simulated by various authors [41–43]. The fluid is accelerated from rest and, at this Reynolds number, attains steady state conditions; streamfunctions obtained by the proposed CFV formulation on a non-uniform 40×40 grid are shown in Fig. 17. We simulated this flow configuration on both uniform and non-uniform grids, using the standard second-order method and the sixth-order CFV scheme. Results from a simulation, obtained with a standard second-order finite-volume scheme on a uniform, staggered 192×192 grid, are used as reference; the accuracy of such reference data can be inferred from Figs. 18(a) and (b), where they are compared with results from a spectral DNS by Botella and Peyret [41]. The horizontal and vertical velocity components, obtained by both sixth-order compact and standard second-order schemes, both on uniform or stretched 20×20 grids, are compared in Fig. 19. It is evident that compact schemes lead to much better results, even

Table 4
Absolute error on the velocity field obtained for the simulation of the decaying Taylor–Green vortices

	A	B	C
10×10	2.03e−4	5.71e−6	0.0106
20×20	4.25e−6	3.95e−7	0.0013
40×40	7.26e−8	2.45e−8	1.194e−4

A: CFV sixth-order scheme with Dirichlet boundary conditions and with uniform grids; B: CFV fourth-order scheme with periodic boundary conditions and with uniform grids; C: CFV sixth-order method with Dirichlet boundary conditions and with non-uniform grids.

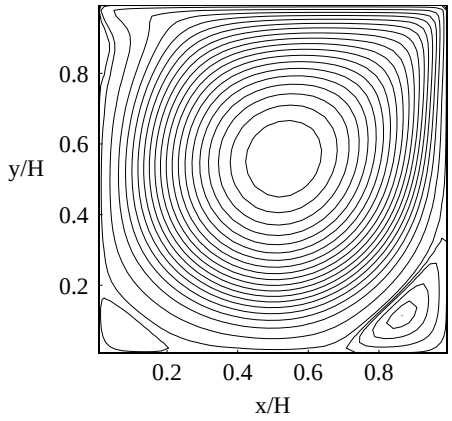

Fig. 17. Streamlines for the lid-driven cavity flow at $Re = 1000$, evaluated by the sixth-order CFV algorithm on a non-uniform 40×40 grid.

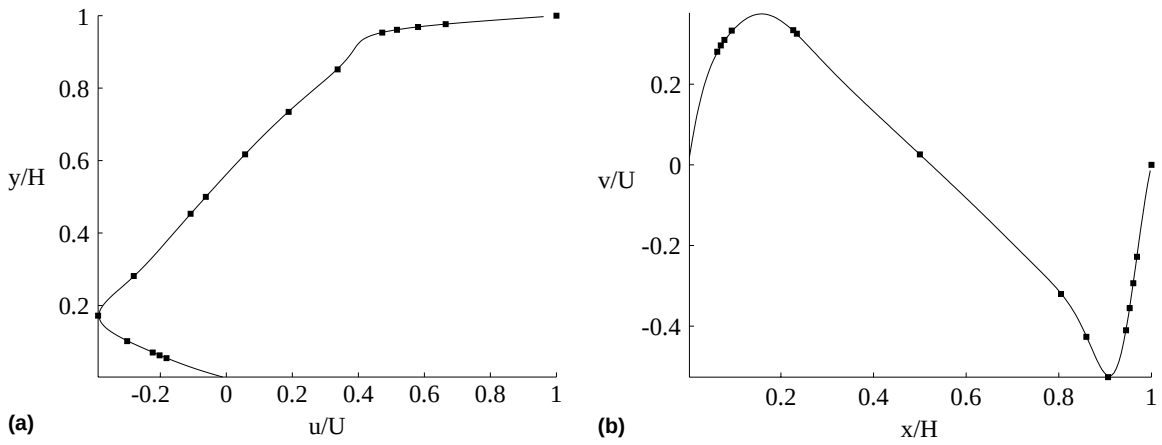

Fig. 18. Comparison of results from two simulations of the lid-driven cavity at $Re = 1000$. The solid line represents data from a second-order finite-volume simulation on a uniform 192×192 staggered grid; the symbols show results of a spectral DNS by Botella and Peyret [41]. (a) Horizontal velocity component on the cavity vertical axis. (b) Vertical velocity component on the cavity horizontal axis.

on such a coarse grid. Moreover, the grid stretching leads to improved results, regardless to the spatial discretization used; this shows that the proposed formulation for dealing with non-uniform Cartesian grids is effective.

6.5. Two-dimensional lid-driven cavity at $Re = 5000$

The simulation of a lid-diven cavity flow at $Re = 5000$ is used as a more severe test for the robustness of the proposed method. The flow is laminar and steady, in that transition occurs approximately at Reynolds greater than 7500 [42]; nevertheless, this test case clearly proves a certain lack of robustness of the method, compared to the ST2 scheme with a staggered grid arrangement. This is a common problem with high-order compact schemes, and is related to the high-resolution characteristics of compact schemes at large wave-

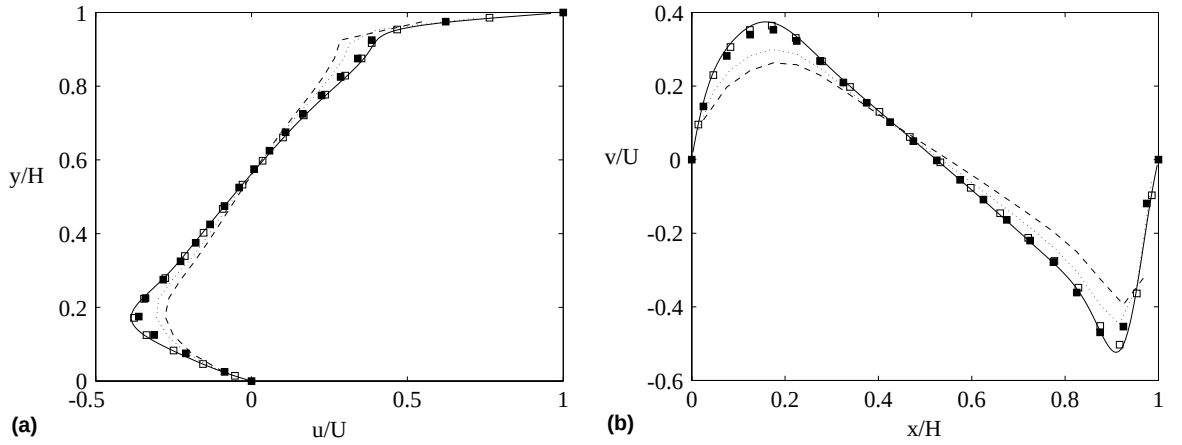

Fig. 19. Comparison of results from several finite-volume simulations of the lid-driven cavity at $Re = 1000$. Solid line: second-order scheme on a uniform 192×192 staggered grid; dashed line: second-order scheme on a uniform 20×20 staggered grid; dotted line: second-order scheme on a non-uniform 20×20 staggered grid; black squares: sixth-order CFV scheme on a uniform 20×20 staggered grid; white squares: sixth-order CFV scheme on a non-uniform 20×20 staggered grid. (a) Horizontal velocity component on the cavity vertical axis; (b) vertical velocity component on the cavity horizontal axis.

numbers, which renders them more sensitive to aliasing errors [16]. In addition, kinetic energy conservation is still an open issue for high-order compact schemes, which therefore lack a strong constraint for limiting the onset of instabilities. High-order compact filtering [7,19] is a well-established practice for the *stabilization* of compact schemes in incompressible fluid flow simulations and we use a sixth-order filter, as proposed by Lele [7]

$$\beta\widetilde{f}_{j-2} + \alpha\widetilde{f}_{j-1} + \widetilde{f}_j + \alpha\widetilde{f}_{j+1} + \beta\widetilde{f}_{j+2} = a\widetilde{f}_j + \frac{b}{2}\left(f_{j-1} + f_{j+1}\right) + \frac{c}{2}\left(f_{j-2} + f_{j+2}\right) + \frac{d}{2}\left(f_{j-3} + f_{j+3}\right). \tag{94}$$

The transfer function of (94) is:

$$T(k\Delta x) = \frac{a + b\cos(k\Delta x) + c\cos(2k\Delta x) + d\cos(3k\Delta x)}{1 + 2\alpha\cos(k\Delta x) + 2\beta\cos(2k\Delta x)}. \tag{95}$$

The coefficients in (94) are determined by imposing the following conditions:

$$T(0) = T(\pi) = 0,$$
$$T''(0) = T^{\mathrm{IV}}(0) = T''(\pi) = 0,$$
$$T(a^*\pi) = T^*.$$

The resulting coefficients are functions of a^* and T^*: the closer are a^* to π and T^* to 1, the sharper is the filter. The transfer function (95) is represented in Fig. 20, for several values of the coefficients a^* and T^*. Near-wall filtering was either neglected or performed by the symmetric scheme (94), using extrapolated values at *ghost* points.

Fig. 21 shows traces of the volume-averaged kinetic energy, acquired during two simulations performed on a 20×20 non-uniform grid at $Re = 5000$. Both simulations assume a zero-velocity field as initial condition; the kinetic energy trace for the filtered flow field attains a plateau, while in the unfiltered simulation the kinetic energy accumulates within the computational domain.

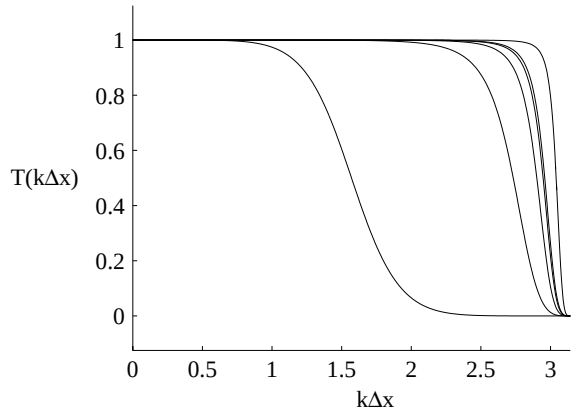

Fig. 20. Transfer function for the compact filter (94), for different values of a^* and T^*.

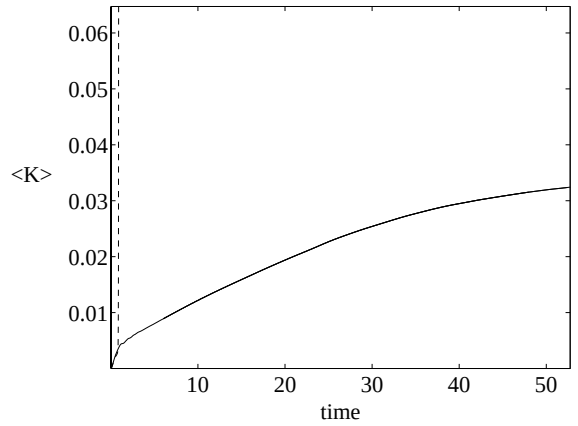

Fig. 21. Traces of the volume-averaged kinetic energy for the lid-driven cavity at $Re = 5000$, sampled during two simulations performed on a 20×20 non-uniform grid. Solid line: filtered; dashed line: unfiltered.

In Table 5 we report the minimum value of the streamfunction in the computational domain, evaluated on several uniform grids by both the filtered CFV and the ST2 schemes. In processing the results for all simulations, the streamfunction was evaluated by solving a Poisson equation to second-order accuracy. This approach is consistent with the remark that the minimum of the streamfunction can be evaluated at most with second-order accuracy, on a discrete computational grid. This is not a major drawback, since we aim just to show that the proposed methodology converges to the correct solution even in simulating a quite complex flow; in addition these results allow for a rough comparison between the accuracy of the proposed compact finite-volume schemes and that of the standard second-order finite-volume method. In all the simulations with the compact schemes, the coefficients a^* and T^* were assumed as 0.95 and 0.95, corresponding to a very sharp filter.

6.6. *Differentially heated cavity at* $Pr = 0$

The simulation of a differentially heated cavity flow is performed to investigate the capability of the proposed CFV method to reproduce unsteady phenomena within closed domains. The geometry and

Table 5
Minimum value of the streamfunction for the lid-driven cavity at $Re = 5000$

Grid	CS	ST2
40×40	−0.0578776	−0.0448441
80×80	−0.0606934	−0.0545659
160×160	−0.0621273	−0.0599278
320×320	−0.0626347	−0.0618647

CS refers to the proposed sixth-order compact method. ST2 refers to the standard second-order finite-volume method. The streamfunction is zero on the boundary.

boundary conditions are illustrated in Fig. 22, representing a rectangular cavity of height H and length $L = 4H$. Top and bottom walls are adiabatic ($\partial T/\partial n = 0$) and vertical surfaces are kept at constant uniform temperature. The left wall is warm at temperature T_h while the right wall is cold at temperature T_c. The temperature scale is defined as the difference between the warm and cold wall, i.e. $\Delta T = T_h - T_c$. The boundary conditions are summarized in (96)

$$\begin{aligned} &\mathbf{u} = 0 \quad \text{at } x = 0, L, \;\; y = 0, H, \\ &T = T_h \quad \text{at } x = 0, \\ &T = T_c \quad \text{at } x = L, \\ &\partial T/\partial n = 0 \quad \text{at } y = 0, H. \end{aligned} \tag{96}$$

The Grashof number equals 1.2×10^5, where Gr is based on the cavity height. Infinite thermal diffusivity is assumed, and thus the value of the Prandtl number is zero. Advection is therefore negligible and the enthalpy equation yields the following temperature distribution:

$$T = T(x) = T_c + \frac{x}{L}(T_h - T_c). \tag{97}$$

Practically, the energy equation is not solved in the computations, but rather the solution for the temperature field (97) is inserted as the buoyancy term into the momentum equations, using the Boussinesq approximation. For this value of Gr the flow displays an oscillatory behavior, with a known frequency [42].

The computations are performed with the Crank–Nicolson/Adams–Bashforth time-stepping scheme, with $\Delta t = 0.0005$, corresponding to a maximum CFL number of 0.015, which ensures that the time discretization errors are negligible. Two uniform grids are considered, namely a 64×16 and a 128×32. Both grids lead the correct oscillatory behavior. Characteristic flow patterns at different time instants are shown

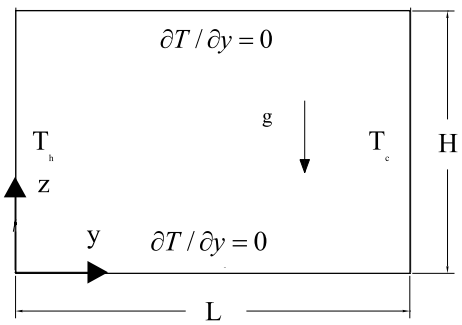

Fig. 22. Schematic representation of the differentially heated cavity.

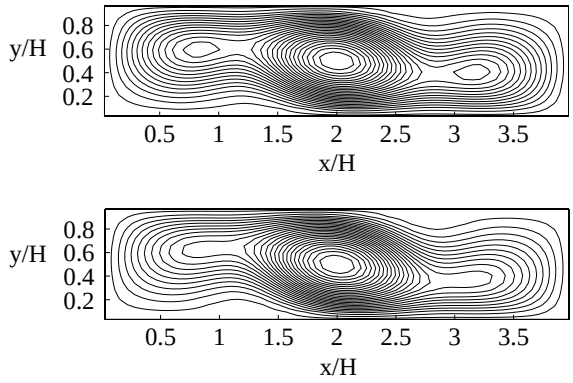

Fig. 23. Flow patterns in the differentially heated cavity; results of a simulation with the sixth-order CFV scheme, on a uniform 64×16 grid.

Table 6
Comparison of various quantities for the differentially heated cavity flow

Scheme	Grid	u_{max}	v_{max}	$f \times 10^2$
CFV sixth-order	64×16	0.45865	0.45141	5.372
	128×32	0.47019	0.4589	5.175
Nobile [42]	128×32	0.4624	0.4401	4.981
	256×64	0.4689	0.4552	5.078
Behnia et al. [43]	321×81	0.4694	0.4577	5.159

u_{max} is the maximum horizontal velocity at $x/H = 1$; v_{max} is the maximum vertical velocity at $y/H = 0.5$; f is the time-frequency of the most energetic mode in the Fourier spectrum of a given quantity.

in Fig. 23, for the 64×16 grid. The flow oscillates between one and three vortices patterns, as expected [42,43]. Table 6 compares results of different authors. The maximum values of the velocity components during one complete flow cycle and the dominant oscillation frequency are usually reported for comparison. The scattering of the results reported in Table 6 confirms that such data are not suitable for accuracy comparisons. However, all data are sufficiently close to each other, to state that the proposed CFV method is able to simulate complex transient phenomena.

7. Concluding remarks

Compact spatial-discretization schemes are a state-of-the-art technology in the numerical simulation of turbulent flows, since they combine high resolution with short computational stencils. While compact finite-difference methods have been extensively used in direct and large eddy simulations of both compressible and incompressible flows, the development of compact finite-volume algorithms is quite recent. Papers by Pereira et al. [18], Kobayashi [25], Kim and Lee [24] and Smirnov et al. [19] provide some guidelines, in that they select cell-averaged quantities as main unknowns, propose fully coupled solution strategies for the Navier–Stokes equations and address the issue of spectral-like compact schemes. While Pereira et al. [18] devote a marginal part of their work to the extension of CFV schemes to general coordinate systems, papers by Smirnov et al. [19,35] report extensively on this issue, by presenting results of several two- and three-

dimensional flow simulations on both Cartesian and boundary-fitted grids. They do not introduce metrics, and work directly in the physical space.

All papers cited above refer to collocated grid arrangements. The main contribution of our work is the introduction of Cartesian, non-uniform staggered grids. In the paper, we provide our view about the usefulness of introducing the staggered grid arrangement in the development of CFV methods. Though further investigation is needed in order to adequately investigate the properties of compact finite-volume schemes on staggered grids, with particular reference to the issue of kinetic-energy conservation, results by other authors suggest that the staggered arrangement could be beneficial in improving the robustness and conservation properties of compact schemes [16]. Pereira et al. [18] show that, under particular assumptions, it is possible to avoid velocity–pressure decoupling, in the framework of collocated fourth-order CFV schemes, by simply using odd numbers of nodes along each computational direction; both Pereira et al. [18] and Smirnov et al. [19,35] verify that such approach leads to oscillations-free velocity fields, even in more general conditions. Nevertheless, the staggering is, up to date, the only *inherent* cure for avoiding the velocity–pressure decoupling, regardless the number of nodes and the type of boundary conditions.

Even in the simple framework of Cartesian grids, we proved the usefulness of coordinate transformations in order to apply the CFV method on non-uniform grids. The compact differentiation and interpolation schemes developed on uniform grids can be directly applied to non-uniform grids, in order to approximate both the physical quantities and, in case, the metrics. Of course, the use of coordinate transformations is not free of drawbacks. Some care must be taken in the discretization of metrics [33], in order to avoid instabilities. In addition, results by other authors indicate that developing the compact schemes directly on the physical grid, thus using variable coefficients in the compact equations, leads to very accurate results even on grids affected by severe non-uniformity [36]. Nevertheless, results by other authors indicate that the introduction of coordinate transformations is required, in order to derive energy-conserving schemes [13,15,37]; in addition, we show that, though the FIM approach allows to obtain convergent results even on random grids, while the JT method does not, on smoothly varying meshes both methods lead to comparable accuracy. Moreover, the use of metrics makes clear that 1D compact schemes can be used, even in multi-dimensional problems.

Segregated schemes are widely adopted in direct and large eddy simulation of turbulent flows, since large computational savings can be obtained from the serial solution of momentum and continuity equations. We propose a CFV segregated method based on the Projection 2 fractional-step algorithm by Gresho [28], which proved to be effective in the simulation of both steady and unsteady flows. The key point of our approach is the bijective compact relation between cell-averaged and face-averaged quantities. In addition, we verify that a second-order discretization of Poisson's equation for pseudo-pressure does not deteriorate the order of accuracy of higher-order methods, since the second-order spatial error is scaled by $(\Delta t)^2$, while it vanishes if using an iterative fractional-step approach.

The use of semi-implicit time-stepping schemes requires the simultaneous solution of compact differentiation equations and momentum equations. We propose an efficient algorithm based on the Alternate Direction Implicit method [17], coupled with a direct solver for *almost*-banded coefficient matrices, presented in Appendix B. The off-diagonal quantities, arising from the compact discretization of the transient term $\mathbf{u}^{n+1}$, are treated by deferred correction, in order to maintain the direction-splitting of the ADI method.

Spectral-like schemes recognize the importance of resolution characteristics, with respect to asymptotic accuracy. We develop and test spectral-like schemes for both interpolation and differentiation, based on the usual least-squares approach [19,25]. The advection of a sharp cone around a circular path is used in order to show the superior characteristics of this method with respect to a fourth-order *traditional* compact scheme, and its slightly better behavior even with respect to a compact sixth-order method, at least when the test case is reproduced on a rather coarse grid.

We show that CFV symmetric schemes are prone to develop unphysical oscillations, for excessively large values of the cell-Péclet number. Spectral-like schemes prove to perform even worse than *traditional* CFV schemes, in this respect. The compact filtering by Lele [7] is efficient in damping wiggles; the combination of the spectral-like CFV scheme with a fourth-order compact filtering seems particularly appealing, in this respect. The simulation of the lid-driven cavity at $Re = 5000$ serves as a more severe test for evaluating the robustness of the proposed compact method. While on fine enough grids there is no need of any filtering procedure, in order to obtain stable simulations, on coarse grids, a compact high-order filtering is effective in stabilizing the computation, without sensibly affecting the accuracy of the results.

Acknowledgements

Financial support for this research was provided by MIUR – Progetto di Ricerca di Interesse Nazionale 2001, *Convezione Monofase Naturale e Mista: Aspetti Fondamentali ed Applicazioni in Componenti e Sistemi Termici*, and by ENEA – Contract *Settore Calcolo* L. 95/95, and is gratefully acknowledged.

Appendix A. Extension to three dimensions

The compact equations derived in this paper can be easily extended to the three-dimensional case. As an example, we present the evaluation of the advective flux of u momentum across the upper $z =$ constant face of a u-staggered control volume, which, with the present notation, is indicated by $\overline{uw}^{xy}_{i+1/2,j,k+1/2}$. A uniform grid is assumed. The location of some representative variables, involved in the evaluation of this term, is indicated in Fig. 24. We derive only symmetric equations to be used in the interior of the computational domain.

The $\overline{uw}^{xy}_{i+1/2,j,k+1/2}$-momentum flux is defined by a double integration

$$\overline{uw}^{xy}_{i+1/2,j,k+1/2} = \frac{1}{\Delta x \Delta y} \int_{x_i}^{x_{i+1}} \int_{y_{j-1/2}}^{y_{j+1/2}} u\left(x, y, z_{k+1/2}\right) w\left(x, y, z_{k+1/2}\right) \mathrm{d}x \, \mathrm{d}y. \tag{A.1}$$

The integral in (A.1) can be approximated, to fourth-order accuracy, by the two-dimensional equation (49), or by the one-dimensional scheme (56). If using (56), symmetry reasons would suggest to approximate (A.1) by the average of (56), evaluated both along x and y:

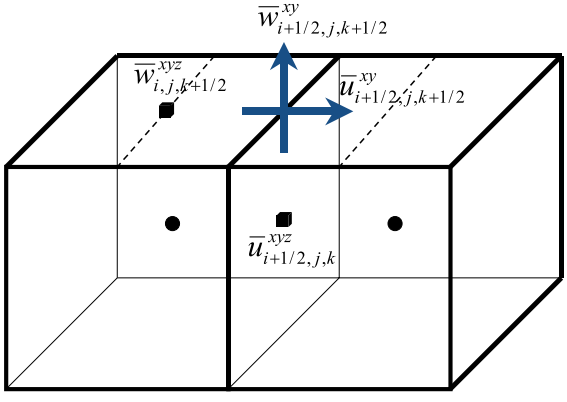

Fig. 24. Three-dimensional control volumes, reporting the location of some unknowns.

$$
\begin{aligned}
&a_{43}\overline{uw}^{xy}_{i+3/2,j,k+1/2} + \overline{uw}^{xy}_{i+1/2,j,k+1/2} + a_{43}\overline{uw}^{xy}_{i-1/2,j,k+1/2} \\
&\quad = a_{44}\overline{u}^{xy}_{i+1/2,j,k+1/2}\overline{w}^{xy}_{i+1/2,j,k+1/2} + a_{45}\left[\overline{u}^{xy}_{i+3/2,j,k+1/2}\overline{w}^{xy}_{i+3/2,j,k+1/2} + \overline{u}^{xy}_{i-1/2,j,k+1/2}\overline{w}^{xy}_{i-1/2,j,k+1/2}\right] \\
&\qquad + a_{46}\left[\overline{u}^{xy}_{i+3/2,j,k+1/2}\overline{w}^{xy}_{i+1/2,j,k+1/2} + \overline{u}^{xy}_{i+1/2,j,k+1/2}\overline{w}^{xy}_{i+3/2,j,k+1/2} + \overline{u}^{xy}_{i-1/2,j,k+1/2}\overline{w}^{xy}_{i+1/2,j,k+1/2}\right. \\
&\qquad \left. + \overline{u}^{xy}_{i+1/2,j,k+1/2}\overline{w}^{xy}_{i-1/2,j,k+1/2}\right] + a_{47}\left[\overline{u}^{xy}_{i+3/2,j,k+1/2}\overline{w}^{xy}_{i-1/2,j,k+1/2} + \overline{u}^{xy}_{i-1/2,j,k+1/2}\overline{w}^{xy}_{i+3/2,j,k+1/2}\right],
\end{aligned}
$$

$$
\begin{aligned}
&a_{43}\overline{uw}^{xy}_{i+1/2,j+1,k+1/2} + \overline{uw}^{xy}_{i+1/2,j,k+1/2} + a_{43}\overline{uw}^{xy}_{i+1/2,j-1,k+1/2} \\
&\quad = a_{44}\overline{u}^{xy}_{i+1/2,j,k+1/2}\overline{w}^{xy}_{i+1/2,j,k+1/2} + a_{45}\left[\overline{u}^{xy}_{i+1/2,j+1,k+1/2}\overline{w}^{xy}_{i+1/2,j+1,k+1/2} + \overline{u}^{xy}_{i+1/2,j-1,k+1/2}\overline{w}^{xy}_{i+1/2,j-1,k+1/2}\right] \\
&\qquad + a_{46}\left[\overline{u}^{xy}_{i+1/2,j+1,k+1/2}\overline{w}^{xy}_{i+1/2,j,k+1/2} + \overline{u}^{xy}_{i+1/2,j,k+1/2}\overline{w}^{xy}_{i+1/2,j+1,k+1/2} + \overline{u}^{xy}_{i+1/2,j-1,k+1/2}\overline{w}^{xy}_{i+1/2,j,k+1/2}\right. \\
&\qquad \left. + \overline{u}^{xy}_{i+1/2,j,k+1/2}\overline{w}^{xy}_{i+1/2,j-1,k+1/2}\right] + a_{47}\left[\overline{u}^{xy}_{i+1/2,j+1,k+1/2}\overline{w}^{xy}_{i+1/2,j-1,k+1/2} + \overline{u}^{xy}_{i+1/2,j-1,k+1/2}\overline{w}^{xy}_{i+1/2,j+1,k+1/2}\right].
\end{aligned}
$$

The unknown fluxes $\overline{u}^{xy}_{:,j,k+1/2}$ and $\overline{w}^{xy}_{:,j,k+1/2}$ can be obtained by the compact interpolation equations (57) and (59), respectively:

$$
\begin{aligned}
&a_{49}\overline{u}^{xy}_{i+1/2,j,k+5/2} + a_{48}\overline{u}^{xy}_{i+1/2,j,k+3/2} + \overline{u}^{xy}_{i+1/2,j,k+1/2} + a_{48}\overline{u}^{xy}_{i+1/2,j,k-1/2} + a_{49}\overline{u}^{xy}_{i+1/2,j,k-3/2} \\
&\quad = a_{50}\left[\overline{u}^{xyz}_{i+1/2,j,k} + \overline{u}^{xyz}_{i+1/2,j,k+1}\right] + a_{51}\left[\overline{u}^{xyz}_{i+1/2,j,k-1} + \overline{u}^{xyz}_{i+1/2,j,k+2}\right] + a_{52}\left[\overline{u}^{xyz}_{i+1/2,j,k-2} + \overline{u}^{xyz}_{i+1/2,j,k+3}\right],
\end{aligned}
$$

$$
\begin{aligned}
&a_{54}\overline{w}^{xy}_{i+5/2,j,k+1/2} + a_{53}\overline{w}^{xy}_{i+3/2,j,k+1/2} + \overline{w}^{xy}_{i+1/2,j,k+1/2} + a_{53}\overline{w}^{xy}_{i-1/2,j,k+1/2} + a_{54}\overline{w}^{xy}_{i-3/2,j,k+1/2} \\
&\quad = a_{55}\left[\overline{w}^{xy}_{i,j,k+1/2} + \overline{w}^{xy}_{i+1,j,k+1/2}\right] + a_{56}\left[\overline{w}^{xy}_{i-1,j,k+1/2} + \overline{w}^{xy}_{i+2,j,k+1/2}\right] + a_{57}\left[\overline{w}^{xy}_{i-2,j,k+1/2} + \overline{w}^{xy}_{i+3,j,k+1/2}\right].
\end{aligned}
$$

The quantities $\overline{u}^{xyz}$ and $\overline{w}^{xyz}$ are assumed as *main* unknowns and are evaluated from the coupled solution of the conservation and compact equations. The fluxes $\overline{u}^{xy}$ and $\overline{w}^{xy}$ are derived from the *main* unknowns by inverting the bijective relation (65) between cell-averaged values and fluxes; with reference to the w velocity component

$$
\begin{aligned}
&a_{64}\overline{w}^{xy}_{i,j,k+5/2} + a_{63}\overline{w}^{xy}_{i,j,k+3/2} + \overline{w}^{xy}_{i,j,k+1/2} + a_{63}\overline{w}^{xy}_{i,j,k-1/2} + a_{64}\overline{w}^{xy}_{i,j,k-3/2} \\
&\quad = a_{65}\left[\overline{w}^{xyz}_{i,j,k+3/2} + \overline{w}^{xyz}_{i,j,k-1/2}\right] + a_{66}\left[\overline{w}^{xyz}_{i,j,k+5/2} + \overline{w}^{xyz}_{i,j,k-3/2}\right] + a_{67}\overline{w}^{xyz}_{i,j,k+1/2}.
\end{aligned}
$$

Appendix B. Solution of *almost-banded* algebraic linear systems

It was shown that the discretization of the transport equation by a semi-implicit time-stepping scheme, while using compact schemes for the spatial discretization, requires the solution of an algebraic linear system at each time-step, with a characteristic coefficient matrix, represented in Fig. 25. In order to solve the system by an efficient numerical method of linear complexity, we exploited the *almost-banded* structure of the coefficient matrix. For general boundary conditions, this structure involves the first N_1 and the last N_2 full rows, L_b sub-diagonals and U_b upper-diagonals on the remaining rows. The solution procedure extends ideas originally proposed by Temperton [21]. He focused on the solution of cyclic tridiagonal systems. The present method leads to relevant savings in computational time if the solution of many linear systems,

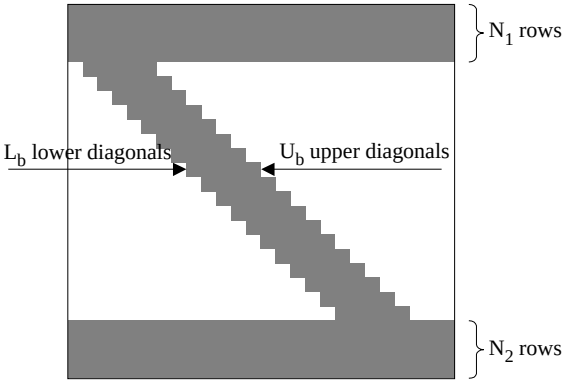

Fig. 25. Coefficient matrix for a *quasi-banded* linear system.

sharing the same coefficient matrix, is required. This circumstance is motivated by the relevant number of operations required in the initialization phase. The main points of the method are outlined next.

The initialization phase has to be performed once and for all at the beginning of the simulation, and consists of the following substeps:

(1) Inversion of the coefficient matrix $\mathbf{A} = (a_{i,j})$; iterative methods can be convenient in the case of large systems. Store the first N_1 and the last N_2 rows of the inverse matrix $\mathbf{B} = (b_{ij}) = \mathbf{A}^{-1}$.
(2) The terms (a_{ij}), $i, j = N_1 + 1 \cdots N - N_2$, define a banded matrix, with $L_b + U_b + 1$ diagonals, and can be stored in packed form [44].
(3) The terms (a_{ij}), $i = N_1 + 1 \cdots N_1 + L_b$, $j = i - L_b \cdots i - 1$, and $i = N - N_2 - U_b + 1 \cdots N - N_2$, $j = i + 1 \cdots i + U_b$, must be stored, since they will *reappear* on the right-hand side.
(4) The bounded matrix stored in (2) can now be factorized, for instance by using LU factorization.

The solution phase, to be repeated each time the right-hand side $\{r_j\}$ is modified, is carried out by the following operations:

(1) Evaluation of the unknowns x_i, $i = 1 \cdots N_1$ and $i = N - N_2 + 1 \cdots N$:

$$x_i = \left(b_{ij}\right) r_j. \tag{B.1}$$

(2) Modification of the right-hand side

$$r_i \leftarrow r_i - \sum_{j=\widetilde{j}(i)}^{\widehat{j}(i)} a_{ij} x_j, \quad i = N_1 + 1 \cdots N_1 + L_b, \quad \widetilde{j}(i) = i - L_b, \quad \widehat{j}(i) = i - 1,$$
$$i = N - N_2 - U_b \cdots N - N_2, \quad \widetilde{j}(i) = i + 1, \quad \widehat{j}(i) = i + U_b. \tag{B.2}$$

(3) Solution of the $(N - N_1 - N_2) \times (N - N_1 - N_2)$ bounded system, for the unknowns x_i, $i = N_1 + 1 \cdots N - N_2$.

References

[1] H. Tennekes, J.L. Lumley, A First Course in Turbulence, MIT Press, Cambridge, MA, 1972.
[2] H.O. Kreiss, S.A. Orszag, M. Israeli, Numerical simulation of viscous incompressible flows, Annual Review of Fluid Mechanics 6 (281) (1974).
[3] R.S. Hirsh, Higher order accurate difference solutions of fluid mechanics problems by a compact differencing technique, Journal of Computational Physics 19 (90) (1975).

[4] Y. Adam, Journal of Computational Physics 24 (10) (1977).
[5] N.N. Mansour, P. Moin, W.C. Reynolds, J.H. Ferziger, Turbulent Shear Flows I, Springer, Berlin, 1977.
[6] S.G. Rubin, P.K. Khosla, Polynomial interpolation methods for viscous flow calculations, Journal of Computational Physics 24 (217) (1977).
[7] S.K. Lele, Compact finite difference schemes with spectral-like resolution, Journal of Computational Physics 103 (1992) 16–42.
[8] M. Meinke, W. Schröder, E. Krause, Th. Rister, A comparison of second- and sixth-order methods for large-eddy simulations, Computers and Fluids 31 (2002) 695–718.
[9] M.S. Liou, C.J. Steffen, A new flux splitting scheme, Journal of Computational Physics 107 (1993) 23–39.
[10] L. Jiang, H. Shan, C. Liu, Direct numerical simulation of boundary-layer receptivity for subsonic flow around airfoil, in: Recent advances in DNS and LES Proceedings of the Second AFOSR Conference held at Rutgers, Kluwer Academic Publishers, Dordrecht, 1999.
[11] M.R. Visbal, D.V. Gaitonde, High-order accurate methods for unsteady vortical flows on curvilinear meshes, AIAA Paper, 1998, pp. 98–131.
[12] B.J. Boersma, Direct numerical simulation of jet noise, in: DNS/LES Progress and Challenges Proceedings of the Third AFOSR International Conference, Greyden Press, 2001, pp. 589–596.
[13] Y. Morinishi, T.S. Lund, O.V. Vasilyev, P. Moin, Fully conservative higher order finite difference schemes for incompressible flow, Journal of Computational Physics 143 (1998) 90–124.
[14] F.H. Harlow, J.E. Welch, Numerical calculation of time-dependent viscous incompressible flow of fluid with free surface, Physics of Fluids 8 (12) (1965) 2182–2189.
[15] O.V. Vasilyev, High-order finite difference schemes on non-uniform meshes with good conservation properties, Journal of Computational Physics 157 (2000) 746–761.
[16] S. Nagarajan, S.K. Lele, J.H. Ferziger, A robust high-order compact method for large eddy simulation, Journal of Computational Physics 191 (2003) 392–419.
[17] J.H. Ferziger, M. Perić, Computational Methods for Fluid Dynamics, Springer, Berlin, 1999.
[18] J.M.C. Pereira, M.H. Kobayashi, J.C.F. Pereira, A fourth-order-accurate finite volume compact method for the incompressible Navier–Stokes solutions, Journal of Computational Physics 167 (2001) 217–243.
[19] S. Smirnov, C. Lacor, M. Baelmans, A finite volume formulation for compact scheme with applications to LES, AIAA Paper 2001-2546, 15th AIAA Computational Fluid Dynamics Conference, June 11–14, Anaheim, CA, 2001.
[20] H. Le, P. Moin, An improvement of fractional step methods for the incompressible Navier–Stokes equations, Journal of Computational Physics 92 (1991) 369–379.
[21] C. Temperton, Algorithms for the solution of cyclic tridiagonal systems, Journal of Computational Physics 19 (1975) 317–323.
[22] Ž. Lilek, M. Perić, A fourth-order finite volume method with collocated variable arrangement, Computers and Fluids 24 (1995) 239–252.
[23] L. Jiang, H. Shan, C. Liu, Weighted compact scheme, in: DNS/LES Progress and Challenges Proceedings of the Third AFOSR International Conference, Greyden Press, 2001, pp. 129–144.
[24] J.W. Kim, D.J. Lee, Optimized compact finite difference schemes with maximum resolution, AIAA Journal 34 (5) (1996) 887–893.
[25] M.H. Kobayashi, On a class of Padé finite volume methods, Journal of Computational Physics 156 (1999) 137–180.
[26] H. Lomax, T.H. Pulliam, D.W. Zingg, Fundamentals of Computational Fluid Dynamics, Springer, Berlin, 2001.
[27] J.D. Anderson, Computational Fluid Dynamics: The Basics with Applications, McGraw-Hill, New York, 1995.
[28] P.M. Gresho, On the theory of semi-implicit projection methods for viscous incompressible flow and its implementation via a finite element method that also introduces a nearly consistent mass matrix. Part 1: theory, International Journal of Numerical Methods for Fluids 11 (1990) 587–620.
[29] S. Armfield, R. Street, An analysis and comparison of the time accuracy of fractional-step methods for the Navier–Stokes equations on staggered grids, International Journal of Numerical Methods for Fluids 38 (2002) 255–282.
[30] V. Babu, S.A. Korpela, On the direct solution of Poisson's equation on a non-uniform grid, Journal of Computational Physics 104 (1993) 93–98.
[31] M.C. Sharatchandra, D.L. Rhode, New, strongly conservative finite-volume formulation for fluid flows in irregular geometries using contravariant velocity components: part 1, theory, Numerical Heat Transfer, Part B 26 (1994) 39–52.
[32] M.C. Sharatchandra, D.L. Rhode, New, strongly conservative finite-volume formulation for fluid flows in irregular geometries using contravariant velocity components: part 2, assessment, Numerical Heat Transfer, Part B 26 (1994) 53–62.
[33] D.V. Gaitonde, J.S. Shang, J.L. Young, Practical aspects of higher-order numerical schemes for wave-propagation phenomena, International Journal for Numerical Methods in Engineering 45 (1999) 1849–1869.
[34] J.C. Tannehill, D.A. Anderson, R.H. Pletcher, Computational Fluid Mechanics and Heat Transfer, second ed., Taylor & Francis, London, 1997.
[35] S. Smirnov, C. Lacor, B. Lessani, J. Meyers, M. Baelmans, A finite volume formulation for compact schemes on arbitrary meshes with applications to RANS and LES, European Congress on Computational Methods in Applied Sciences and Engineering, September 11–14, Barcelona, 2000.

[36] L. Gamet, F. Ducros, F. Nicoud, T. Poinsot, Compact finite difference schemes on non-uniform meshes. Application to direct numerical simulations of compressible flows, International Journal of Numerical Methods for Fluids 29 (1999) 159–191.
[37] R.W.C.P. Verstappen, A.E.P. Veldman, Spectro-consistent discretization of Navier–Stokes: a challenge to RANS and LES, Journal of Engineering Mathematics 34 (1998) 163–179.
[38] The MathWorks, Symbolic Math Toolbox for use with MATLAB®, 1993.
[39] S.V. Patankar, Numerical Heat Transfer and Fluid Flow, Hemisphere Publishing Corporation, New York, 1980.
[40] B.P. Leonard, Elliptic systems: finite difference method iv, in: W.J. Minkowycz, E.M. Sparrow, G.E. Schneider, R.H. Pletcher (Eds.), Handbook of Numerical Heat Transfer, Wiley, New York, 1988, pp. 348–357 (Chapter 9).
[41] O. Botella, R. Peyret, Benchmark spectral results on the lid-driven cavity flow, Computers and Fluids 27 (1998) 421–433.
[42] E. Nobile, Simulation of time-dependent flow in cavities with the additive-correction multigrid method, Numerical Heat Transfer, Part B 30 (1996) 315–370.
[43] M. Behnia, G. de Vahl Davis, F. Stella, G. Guj, A comparison of velocity-vorticity and stream function-vorticity formulations for $Pr = 0$, in: B. Roux (Ed.), Notes in Numerical Fluid Mechanics, vol. 27, Vieweg, Braunschweig, 1990, pp. 25–34.
[44] W.H. Press, B.P. Flannery, S.A. Teukolsky, W.T. Vetterling, Numerical Recipes: The Art of Scientific Computing, second ed., Cambridge University Press, Cambridge, 1992.